Interannual Sea Level Variability along the U.S. East Coast during the Satellite Altimetry Era: Local versus Remote Forcing

YINGLI ZHU,[a] WEIQING HAN,[a] MICHAEL A. ALEXANDER,[b] AND SANG-IK SHIN[b,c]

[a] *Department of Atmospheric and Oceanic Sciences, University of Colorado Boulder, Boulder, Colorado*
[b] *Physical Science Division, NOAA/Earth System Research Laboratory, Boulder, Colorado*
[c] *CIRES, University of Colorado Boulder, Boulder, Colorado*

(Manuscript received 2 February 2023, in final form 27 September 2023, accepted 2 October 2023)

ABSTRACT: The contributions of local and remote forcings to the interannual sea level anomalies (SLAs) along the U.S. East Coast (USEC) during the satellite altimetry era from 1993 to 2019 are quantified with analytical models assisted by statistical methods. The local forcings from alongshore wind stress, sea level pressure via inverted barometer (IB) effect, and river discharges together explain 47%, 60.4%, and 66.8% of coastal sea level variance in the South Atlantic Bight (SAB), Mid-Atlantic Bight (MAB), and Gulf of Maine (GOM), respectively, with river discharges having the minimum contribution. Over a longer period of 1960–2019, the contribution of local forcings reduces significantly, with the IB effect having the minimum contribution. The remote forcings associated with open-ocean signals from the east and from the northern boundary at the Scotian coast together with the Gulf Stream (GS) variability explain 45.7%, 28.5%, and 37.7% of coastal sea level variance in the SAB, MAB, and GOM, respectively, playing a role comparable to that of local forcings in the SAB. The open-ocean sea level signals from 35° to 38°N strongly influence coastal SLAs in the SAB. The coastal SLAs in the SAB are also affected by the upstream GS strength (28°–36°N) and basin-scale wind stress curl anomaly, which is linked to the meridional shift in the downstream GS (74°–68°W). Remote forcings from the subpolar North Atlantic and wind stress curl from the Grand Banks to the Scotian coast influence coastal SLAs in the GOM and MAB via the northern boundary of the USEC at the Scotian coast.

KEYWORDS: Ocean; North America; Sea level; Oceanic waves; Interannual variability

1. Introduction

Coastal flooding, one of the major threats to nearshore regions, has had an upward trend along the U.S. East Coast (USEC) in recent decades (e.g., Gornitz et al. 2001; Neumann et al. 2015; Wahl et al. 2015; Wdowinski et al. 2016). Interannual sea level anomalies (SLAs), superimposed on decadal fluctuations and climate change–induced sea level rise, can affect the frequency and spatial pattern of the coastal flooding (Church et al. 2013; Field et al. 2014; Oppenheimer et al. 2019). Therefore, understanding the causes for interannual SLAs along the USEC is important for making annual projections of high tide flooding (Sweet et al. 2019, 2021) and is the focus of this study.

Previous studies have shown that interannual SLAs along the North American east coast result from both local forcings over the shelf and remote forcings from the open ocean [see the reviews of Han et al. (2019), Ponte et al. (2019), and Woodworth et al. (2019)]. Local forcings include wind stress over the shelf (e.g., Sandstrom 1980; Piecuch et al. 2016), the inverted barometer (IB) effect associated with changes of atmospheric sea level pressure (e.g., Piecuch and Ponte 2015), and river discharges into the coastal ocean (e.g., Meade and Emery 1971; Piecuch et al. 2018). Coastal winds, especially the alongshore wind stress, are a major driving force for interannual SLAs at tide-gauge locations along the USEC north of Cape Hatteras (Blaha 1984; Andres et al. 2013; Li et al. 2014; Woodworth et al. 2014; Piecuch et al. 2016; Kenigson et al. 2018; Diabaté et al. 2021), and the IB effect explains about 25% of interannual sea level variance over 1979–2013 (Piecuch and Ponte 2015). In particular, the response of coastal sea level north of Cape Hatteras to atmospheric forcing over the shelf can explain about 50% of the sea level variance on interannual and longer time scales for the 1980–2010 period (after the IB effect is removed), with wind stress forcing dominating the effect of sea level pressure (Piecuch et al. 2016, 2019). South of Cape Hatteras, the influences of both the alongshore wind stress and the IB effect are much weaker. River discharges have also been shown to affect the USEC sea level (Meade and Emery 1971; Piecuch et al. 2018). Although the barotropic response of coastal sea level to river discharges is likely weak and fast, the steric contribution of river discharges to coastal sea level is associated with slower regional adjustment by means of baroclinic dynamics (Durand et al. 2019). Freshwater discharges to the coastal ocean from rivers change the seawater salinity and density around the coast. The buoyant water generated by river discharge is higher than salty ocean water, leading to increased sea level due to halosteric effects (Piecuch et al. 2018).

While local forcings clearly influence interannual USEC sea level, open-ocean processes may also contribute to SLAs, especially south of Cape Hatteras (e.g., Hong et al. 2000; Piecuch et al. 2016). Existing studies have demonstrated the linkage between a reduction in the Gulf Stream (GS) and Atlantic

Supplemental information related to this paper is available at the Journals Online website: https://doi.org/10.1175/JCLI-D-23-0065.s1.

Corresponding author: Yingli Zhu, yingli.zhu@colorado.edu

DOI: 10.1175/JCLI-D-23-0065.1

meridional overturning circulation (AMOC) and sea level rise north of Cape Hatteras using empirical analysis (e.g., Sallenger et al. 2012; Ezer 2013; Ezer et al. 2013; Kopp 2013; Ezer 2015; Goddard et al. 2015; Chen et al. 2020) and climate model experiments (Bingham and Hughes 2009; Yin et al. 2009; Hu et al. 2011; Hu and Bates 2018). By contrast, some observational studies suggested that the interannual coastal SLAs observed north of Cape Hatteras are not associated with the GS strength because the GS leaves the coast at Cape Hatteras (Andres et al. 2013). More recent studies showed that the GS and AMOC properties are spatially dependent (Rossby et al. 2014; Dong et al. 2019; Ezer 2019), and processes contributing to the coastal SLAs and the GS (or AMOC) variability can be correlated without causal linkage. For example, Piecuch et al. (2019) found that the anticorrelation between AMOC and sea level on the New England coast on interannual time scales reflects the antiphase relationship between Ekman-related AMOC transports and coastal sea level driven by local wind and sea level pressure. Therefore, the causal relationship between the GS or AMOC and the western boundary sea level north of Cape Hatteras remains uncertain (Woodworth et al. 2014; Little et al. 2017; Valle-Levinson et al. 2017; Little et al. 2019).

South of Cape Hatteras, the western boundary current controlled by the open-ocean forcings can have an influence on the USEC sea level. On time scales ranging from a few months to decades, SLAs along the USEC south of Cape Hatteras have been linked to the variability of the Florida Current and GS strength (e.g., Blaha 1984; Ezer 2013) as well as the meridional shift in the GS position (Yin and Goddard 2013; Diabaté et al. 2021). The mechanisms by which the meridional shift in the GS position causes coastal SLAs are unclear. In addition, forcings in the open ocean such as westward propagating Rossby waves can have influence on SLAs along the USEC by changing the western boundary current. Hong et al. (2000) suggested that the decadal coastal SLAs between 18° and 38°N were largely caused by the change of GS transport induced by westward propagating Rossby waves generated by the wind stress curl in the open ocean. Although the GS may affect coastal sea level by changes in its strength, position, or other properties, the GS variability is likely accompanied by large-scale heat convergence or divergence. The large-scale heat exchange between open-ocean gyres could be reflected in interannual to decadal SLAs along the USEC (McCarthy et al. 2015; Volkov et al. 2019). A warmer GS and Florida Current in the South Atlantic Bight (SAB) increases coastal sea level (Domingues et al. 2018; Ezer 2019).

Remote processes unrelated to the GS and AMOC strength are also important on interannual time scales (e.g., Little et al. 2017). North of Cape Hatteras, wind stress curl over the open ocean explains ~15% of the coastal sea level variance due to barotropic processes (Piecuch et al. 2016). The steric height in the open ocean has been related to interannual to decadal coastal SLAs (Dangendorf et al. 2021). Moreover, previous observational analyses, numerical simulations using simple models with and without coastal topography, coupled climate models, and adjoint sensitivity analysis have suggested that SLAs along the North American coast have contributions from interior SLAs propagating to the western boundary via Rossby waves, warm-core rings, and SLAs at higher latitudes (Miller and Douglas 2007; Xu and Oey 2011; Zhai et al. 2014; Minobe et al. 2017; Wise et al. 2018; Wu 2021; Frederikse et al. 2022; Wang et al. 2022). When the open-ocean low-frequency sea level signals reach the western boundary, they can be carried equatorward along the continental slope by coastally trapped waves with part of the signals reaching the west coast under bottom friction (e.g., Wise et al. 2018; Hughes et al. 2019; Wise et al. 2020a,b). In addition, the zonal volume transport into the western boundary has been shown to account for spatially coherent interannual SLAs from the Caribbean to Nova Scotia (Thompson and Mitchum 2014). The SLAs in the Labrador Sea can also be important for the sea level along the USEC north of Cape Hatteras (Xu and Oey 2011; Frederikse et al. 2017).

While remote forcings can significantly affect SLAs, the ways by which they influence the observed sea level along the USEC are not well understood. How is the meridional shift in the GS position linked to coastal SLAs? How much coastal sea level variance can be explained by open-ocean forcings via Rossby waves and by open-ocean forcings via changes in the western boundary current? Although some studies suggested that local atmospheric forcings over the shelf dominate the USEC interannual SLAs north of Cape Hatteras (e.g., Woodworth et al. 2014), the contributions of remote forcings have not been carefully assessed, and the relative importance of local versus remote forcings in affecting SLAs in different regions of the USEC has not been quantified. In this study, we use observed data for the 1993–2019 period to investigate the local versus remote forcing in causing interannual variability of sea level along the USEC. This period is chosen because both tide-gauge and satellite altimetry sea level data are available to reveal the locally forced and remotely generated SLA signals that propagate to the USEC from the open ocean and from higher latitudes via the western boundary. Here, local forcings refer to forcings along the USEC and remote forcings refer to forcings outside of the USEC.

The rest of the paper is organized as follows. In section 2, we describe the datasets and methods used in this study. In section 3, we evaluate the contributions of local forcings from surface wind stress, IB effect, and river discharges along the USEC and quantify the contributions of remote forcings to USEC interannual SLAs. We also explore the mechanisms that explain how the open-ocean sea level signals from regions outside of the USEC affect coastal SLAs along the USEC and how the GS variability is linked to the coastal SLAs in the SAB. Section 4 provides a summary and discussion.

2. Data and methods

a. Data

To document the interannual SLAs along the USEC, we analyzed the tide-gauge monthly mean sea level from the Permanent Service for Mean Sea Level (PSMSL; Holgate et al. 2013). We excluded the tide gauges located in bays and estuaries and selected the tide gauges that are exposed to the open ocean and have data more than 90% of the time for the 1993–2019 period (Fig. 1 and Table S1 in the online supplemental material). We choose the period of 1993–2019 because satellite altimetry sea surface

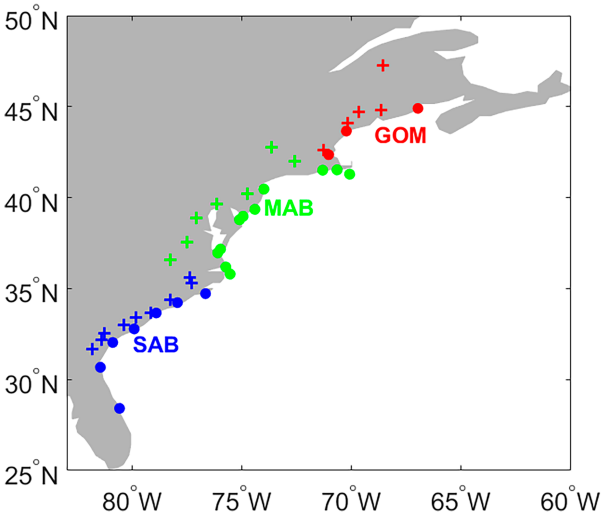

FIG. 1. Locations of tide gauges (filled dots) and river gauges (plus signs). Gauges located in the South Atlantic Bight (SAB), Mid-Atlantic Bight (MAB), and Gulf of Maine (GOM) region are in blue, green, and red, respectively. The GOM is bounded by Nova Scotia in the northeast and by Cape Cod (41.6688°N, 70.2962°W), MA, in the southwest. The MAB region extends from Cape Cod, MA, southward to Cape Lookout off NC. The SAB extends roughly from Cape Hatteras (35.2480°N, 75.5393°W), NC, to West Palm Beach, FL.

height (SSH) data, which are used to provide remotely forced signals for coastal SLAs, are only available since 1993. Using the 27-yr data record, we focus on studying interannual variability of the USEC sea level. Among the many ocean reanalyses, sea level data from the European Centre for Medium-Range Weather Forecasts high-resolution Ocean Reanalysis System 5 (ORAS5) have the longest eddy-permitting record (1958–present), but the ORAS5 SLAs do not agree well with tide-gauge data in the SAB and the Gulf of Maine (GOM) before 1993, a period when satellite altimeter data are not available for ORAS5 to assimilate (see Fig. S1), which may introduce more uncertainties to the remotely forced SLAs. Therefore, in this paper, we primarily focus on the satellite altimetry period beginning in 1993. Even during the satellite era, ORAS5 reanalysis data are not as reliable as altimeter data in depicting open-ocean SLAs used as remote forcings in this study (Fig. S2). In addition, ORAS5 does not assimilate satellite altimetry data in the nearshore environment (i.e., when the ocean bottom depth is shallower than 500 m) and is strongly down weighted within ~800 km of the coastline (Zuo et al. 2019), which is another reason why we mainly focus on the satellite altimetry era instead of a longer period using reanalysis data (e.g., ORAS5) for our analysis. Although the remotely forced coastal SLAs were not examined over a longer period (>27 years) due to the lack of open-ocean observed SLAs before 1993, locally forced coastal SLAs were calculated over a longer period from 1960 to 2019 using high-resolution atmospheric reanalysis data (discussed below) and compared with those obtained for the 1993–2019 period. To compare with the results calculated from atmospheric reanalysis data, we selected the tide gauges with data available more than 70% of the time during 1960–2019 when more tide-gauge data are available relative to the earlier in the twentieth century.

To examine the connection between coastal and open-ocean sea level, we analyzed monthly satellite altimetry data from 1993 to 2019, which were calculated from the 0.25°, daily two-satellite delayed time 2018 (DT2018) sea level dataset provided by the Copernicus Climate Change Service (C3S; Taburet et al. 2019). Unlike the tide-gauge data, satellite altimeters may not accurately measure sea level right at the coast due to land contamination. However, satellite data provide reliable values over the shelf and in the open ocean (Taburet et al. 2019; Cazenave et al. 2022). Therefore, the satellite SSH data are suitable for studying the coastal and open-ocean connection. Since the USEC sea level variability has been linked to basin-scale ocean mass and heat transports (e.g., Thompson and Mitchum 2014; Volkov et al. 2019), we used the 1° × 1° monthly ocean heat content (OHC) data for the 0–2000-m layer (Cheng et al. 2017) to examine large-scale heat redistribution.

To assess the effects of local forcings on interannual SLAs along the USEC, we analyzed monthly surface wind stress, atmospheric sea level pressure, and river discharge data. Monthly wind stress and sea level pressure data, which we used to estimate the IB effect, are from the European Centre for Medium-Range Weather Forecasts reanalysis v5 (ERA5) provided by C3S (Hersbach et al. 2019). The monthly river discharges along the USEC are from the United States Geological Survey (USGS) water data for the nation. The selected rivers in the SAB, the Mid-Atlantic Bight (MAB), and the GOM are the same as those used in Piecuch et al. (2018). For each river, we selected the river gauge that is closest to the ocean and has fewer data gaps (Fig. 1 and Table S2). The remaining data gaps were filled by regressing river discharge at the selected river gauge on upstream sites with a more complete record. Since this paper focuses on the SLAs on interannual time scale, we first removed the mean seasonal cycle and linear trend and then band-pass filtered each dataset to retain variability with periods between 1.5 and 8 years. The regional mean interannual SLAs observed by tide gauges over the period of 1993–2019 have energy peaks at 2.4, 6.6, and 6.6 years in the SAB, MAB, and GOM, respectively.

b. *Methods*

1) ANALYTICAL MODELS OF COASTAL SLA DRIVEN BY LOCAL FORCINGS

In this study, we estimated the influence of local forcings due to the IB effect, alongshore wind stress, and river discharges on interannual SLAs along the USEC with three analytical models. First, the sea level response to sea level pressure was estimated by the IB effect (e.g., Ponte 1992; Wunsch and Stammer 1997; Ponte 2006) with

$$\eta^{\mathrm{IB}} = -\frac{P_a - \overline{P_a}}{\rho g}, \tag{1}$$

where P_a is the sea level pressure, $\overline{P_a}$ is the spatially averaged sea level pressure over the global ocean, ρ is the seawater

density with a constant value of 1025 kg m^{-3}, and g is the acceleration of gravity. The grid point that is nearest to each tide gauge was used for the estimation.

Second, we used a simple, barotropic coastal ocean model (e.g., Hong et al. 2000; Li and Clarke 2005) to evaluate the role of alongshore wind stress forcing in driving USEC SLAs. The barotropic coastal ocean model is given by

$$\frac{\partial \eta^{\tau}}{\partial s} + \lambda \eta^{\tau} = \frac{\tau^{s}}{\rho g H}, \tag{2}$$

where s is the alongshore distance, H is the water depth, τ^s refers to the alongshore wind stress, and $\lambda = \mu/(fHL)$, where f is the Coriolis parameter, L is the shelf width, and μ is the linear bottom friction coefficient. We chose representative values of $\mu = 4 \times 10^{-4}$ m s^{-1}, $H = 30$ m, and $L = 60$ km in the model. The term η^{τ} was estimated by integrating the alongshore wind stress along the coast from the northern boundary of the USEC that is chosen at 44.375°N on the Scotian coast. The model results do not significantly change when choosing μ in the range of 3–6 $\times 10^{-4}$ m s^{-1}, H in the range of 20–50 m, and L in the range of 40–80 km.

Third, halosteric SLAs are generated when the buoyant water induced by fresh river water is transported along the coast. The effect of river discharge on coastal SLAs was estimated with the expression proposed by Piecuch et al. (2018):

$$\eta^{R} = \left(\frac{2f\alpha S_0 Q_F}{g}\right)^{1/2}, \tag{3}$$

where α is the haline contraction coefficient, S_0 is the salinity of the ambient coastal ocean, and Q_F is the volumetric river discharge rate. We used representative values of $S_0 = 35$ practical salinity units (PSUs) and $\alpha = 8 \times 10^{-4}$ psu^{-1}. The value of η^R was estimated with the river discharge Q_F in the SAB, the MAB, and the GOM, respectively.

2) Analytical model of coastal SLAs driven by remote forcings

To quantify the influence of the open-ocean SLAs propagating westward onto the western boundary and remote SLAs at the northern boundary of the USEC, we use the analytical solution of Minobe et al. (2017) for wave propagation that neglects bottom topography,

$$\eta(y, t) = \frac{f(y)}{f_P}\eta(y_P, t) + f(y)\int_{y}^{y_P} \frac{\beta}{f^2}\eta_I[x_I(y'), y', t - \delta(y')]dy', \tag{4}$$

where η is the coastal sea level, η_I is the open-ocean sea level, y_P is the meridional position of the northern boundary, y is the meridional position south of the northern boundary, x_I is the zonal position in the open ocean, β is the meridional variation of the Coriolis parameter, and δ is the time lag that sea level signals take to travel from the open-ocean position, x_I, to the coast. The first and second terms on the right-hand side of Eq. (4) are, respectively, the contributions from the northern boundary, denoted by η^N, and from the open ocean between latitudes y and y_P, denoted by η^W. The northern boundary location is chosen at 44.375°N near the Scotian coast. Forcings from the northern boundary [$\eta(y_P, t)$] and the open ocean (η_I) are derived from satellite altimetry data. Satellite data are chosen for $\eta(y_P, t)$ because there are no continuous tide-gauge records available during the study period. Since satellite-observed SLAs at the northern boundary are from the grid point closest to the coast instead of right on the coast to avoid land contamination, this slight shift in location away from the coast may introduce errors to the estimated coastal SLAs along the USEC; however, the satellite-observed SLAs at the northern boundary are significantly correlated with tide-gauge data at 44.6667°N of the Scotian coast during their overlapping periods (not shown), lending us confidence for using satellite data to provide $\eta(y_P, t)$.

3) Regression model of coastal SLAs driven by Gulf Stream variability

The GS was separated into upstream and downstream components, which are located to the south and north of Cape Hatteras, respectively. Their location and strength indices were estimated from satellite altimetry data by averaging the center location and strength of the upstream GS between 28° and 36°N and the downstream GS between 74° and 68°W (see the appendix for details). The coastal SLA that cannot be accounted for by the analytical models of Eqs. (1)–(4), referred to as residual coastal SLA and denoted by η^{Residual}, is used to estimate the GS influence with a regression model:

$$\eta^{\text{Residual}} = b_0 + b_1 \text{GS}^{\text{up}} + b_2 \text{GS}^{\text{down}} + e, \tag{5}$$

where $\eta^{\text{Residual}} = \eta^{\text{OBS}} - \eta^{\text{IB}} - \eta^{\tau} - \eta^{R} - \eta^{W} - \eta^{N}$, GS^{up} is the upstream GS strength, GS^{down} is the downstream GS location, e is the error, and η^{OBS} represents the tide-gauge-observed SLA. The fitted coastal sea level due to the GS from Eq. (5) is denoted by η^{GS}. The reasons for choosing upstream GS strength and downstream GS location as predictors in Eq. (5) are discussed later in section 3b.

3. Results: Roles of local and remote forcings

In this section, we first assess the effects of local forcings from sea level pressure (i.e., IB effect), alongshore wind stress, and river discharge on coastal SLAs along the USEC (section 3a), using the analytical models described in Eqs. (1)–(3) of section 2b. Then, we estimate the role of remote forcings (section 3b), using an analytical model driven by westward propagating open-ocean signals and high-latitude signals through the northern boundary of the USEC [Eq. (4) of section 2b], together with a regression model that relates the coastal SLA to the GS variability [Eq. (5)].

a. *Local forcings*

Although local forcings have been studied extensively, it is still important to quantify their impacts here in order to assess the relative importance of local versus remote forcings on interannual SLAs in different regions of the USEC.

Correlation coefficients between the tide-gauge-observed and alongshore wind stress–induced SLAs (η^{τ}) from 1993 to

TABLE 1. Percentages of sea level variance (%) explained by different forcings averaged in the SAB, the MAB, and the GOM, respectively, for the 1993–2019 period. The percentage of explained sea level variance is defined as $\mathrm{VARF} = \{1 - [\mathrm{var}(\eta^{\mathrm{OBS}} - \eta^{\mathrm{EST}})/\mathrm{var}(\eta^{\mathrm{OBS}})]\} \times 100\%$, where var represents the computing variance and η^{OBS} and η^{EST} represent the tide-gauge-observed and estimated SLAs, respectively. For the variance of local forcing, we first calculate the sum of SLAs driven by longshore wind stress η^{τ}, the IB effect due to sea level pressure anomaly η^{IB}, and the river effect η^{R}, $\eta^{\mathrm{Local}} = \eta^{\tau} + \eta^{\mathrm{IB}} + \eta^{R}$, and then compute the variance. Variances of remote forcing and total forcing, η^{Remote} and η^{Total}, are calculated in the same manner. Note that $\eta^{\mathrm{Remote}} = \eta^{W} + \eta^{N} + \eta^{\mathrm{GS}}$, where η^{W} and η^{N} are the remotely forced coastal sea level due to westward propagating open-ocean signals and high-latitude signals through the northern boundary, respectively, and η^{GS} is the GS-induced coastal sea level. The total forced coastal sea level is $\eta^{\mathrm{Total}} = \eta^{\mathrm{Local}} + \eta^{\mathrm{Remote}}$.

Region	η^{τ}	η^{IB}	η^{R}	η^{Local}	η^{W}	η^{N}	η^{GS}	η^{Remote}	η^{Total}
SAB	32.7	13.6	8.8	47.0	19.0	7.4	22.7	45.7	77.8
MAB	41.4	31.0	7.2	60.4	1.0	29.9	0.0	28.5	68.1
GOM	46.9	32.1	4.0	66.8	0.1	38.2	0.0	37.7	80.4

2019 are statistically significant ($p \leq 0.1$, where p is the p value of the statistical test for the correlation coefficient) in all three USEC regions (Fig. S3). Given that the smallest decorrelation time scale is 1.5 years due to bandpass filtering and that the data length is 27 years, a conservative effective degree of freedom is given by 27 years/1.5 years = 18. Correlation coefficients with absolute value larger than 0.4 are statistically significant ($p \leq 0.1$). Local alongshore wind stress accounts for 32.7%, 41.4%, and 46.9% of variance of sea level averaged in the SAB, MAB, and GOM, respectively (Table 1). The SLAs due to the IB effect (η^{IB}) are significantly correlated with the tide-gauge-observed SLAs (η^{OBS}) north of Cape Hatteras in the MAB and GOM ($p \leq 0.1$), but the correlation is below the significance level in the SAB (Fig. S3). The IB effect explains 13.6%, 31%, and 32.1% SLA variance in the SAB, MAB, and GOM, respectively (Table 1). Although the observed SLA magnitude, measured by the standard deviation, is larger south of Cape Hatteras (i.e., SAB) compared to north of Cape Hatteras (MAB and GOM), the SLAs induced by local alongshore wind stress and IB effect are both larger and account for more observed variance north of Cape Hatteras (Table 2). These results suggest that local variability of atmospheric circulation over the U.S. east shelf plays an increasingly important role from the SAB to the GOM in causing interannual SLAs along the USEC. Compared to alongshore wind stress and the IB effect, river discharges have much smaller contributions (η^{R}) to the observed coastal SLAs overall (Tables 1 and 2).

The linear superposition of the individual effects estimated above, $\eta^{\mathrm{Local}} = \eta^{\mathrm{IB}} + \eta^{\tau} + \eta^{R}$, represents the effect of total local forcings. Locally forced and observed SLAs are significantly correlated ($p \leq 0.1$) at all tide gauges. The three local forcings together explain 47.0%, 60.4%, and 66.8% of variance of sea level averaged in the SAB, MAB, and GOM, respectively (Table 1), suggesting the importance of local

TABLE 2. Standard deviations (mm) of observed SLAs and estimated SLAs driven by different forcings averaged in the SAB, MAB, and GOM, respectively, for 1993–2019.

Region	η^{OBS}	η^{τ}	η^{IB}	η^{R}	η^{Local}	η^{W}	η^{N}	η^{GS}	η^{Remote}	η^{Total}
SAB	24.3	8.5	6.9	3.9	13.5	5.9	6.6	8.1	12.9	21.1
MAB	22.6	12.2	7.7	4.2	18.0	2.0	7.7	0.0	8.5	22.3
GOM	21.4	13.8	7.8	2.2	18.2	0.4	8.5	0.0	8.6	22.7

forcings, especially by wind stress and atmospheric sea level pressure, in driving the interannual SLAs along the entire USEC. The simple analytical models used in this study explain a similar amount of coastal sea level variance as obtained from a barotropic ocean model forced by surface air pressure and wind stress (Piecuch et al. 2019). The large contributions of local forcings to the strong interannual SLAs averaged in the SAB, MAB, and GOM, such as the positive SLAs in 2005 and 2010, are clearly seen in Fig. 2 (cf. dashed and solid black lines). The significant influence of local forcings on the SAB interannual SLA differs from the previous study (Hong et al. 2000) that focused on decadal SLA which was largely caused by deep-sea signals over the North Atlantic.

We also examined the locally forced coastal SLAs on interannual time scales during 1960–2019 using ERA5 reanalysis wind and sea level pressure. Compared to the relatively short period of 1993–2019, the locally forced coastal SLAs from 1960 to 2019 show a much smaller IB effect in the MAB and GOM; the contribution from alongshore wind stress is also smaller in the GOM but is larger in the MAB. Overall, the total local forcings play a smaller role in driving the USEC SLAs over the longer period mainly due to the reduced role of the IB effect (Table 3). The standard deviation and time series are shown in Table S3 and Fig. S4. The reduced IB effect for the longer period of 1960–2019 results from the IB's negative contribution in the earlier decades during 1960–86 (Table 3; Zhu et al. 2023). Over the longer period of 1960–2019, the influence of alongshore wind stress dominates over the IB effect in causing USEC sea level variability. Zhu et al. (2023) showed that the IB effect dramatically increased from earlier decades to recent decades especially during boreal summer because the sea level pressure anomalies centered around the MAB, which favor positive contributions to the observed SLAs in the MAB and GOM, become more prominent in recent decades compared to earlier decades. This change in sea level pressure is linked to the variability of the North Atlantic Oscillation [see Zhu et al. (2023) for detailed discussion]. In addition, oceanic processes may also influence the atmospheric wind and pressure pattern other than the NAO on decadal to multidecadal time scales, thereby contributing to the nonstationary role of the local factors.

To confirm our results from the analytical models, we also carried out linear regression analysis to estimate the locally forced coastal SLAs for 1993–2019 (Fig. S5), as in previous studies (e.g., Dangendorf et al. 2014; Frederikse et al. 2017; Diabaté et al. 2021). Both the analytical models and the regression models suggest the importance of local forcings in causing interannual SLAs along the USEC; however, about 30%–50% of SLA variance cannot be explained by local

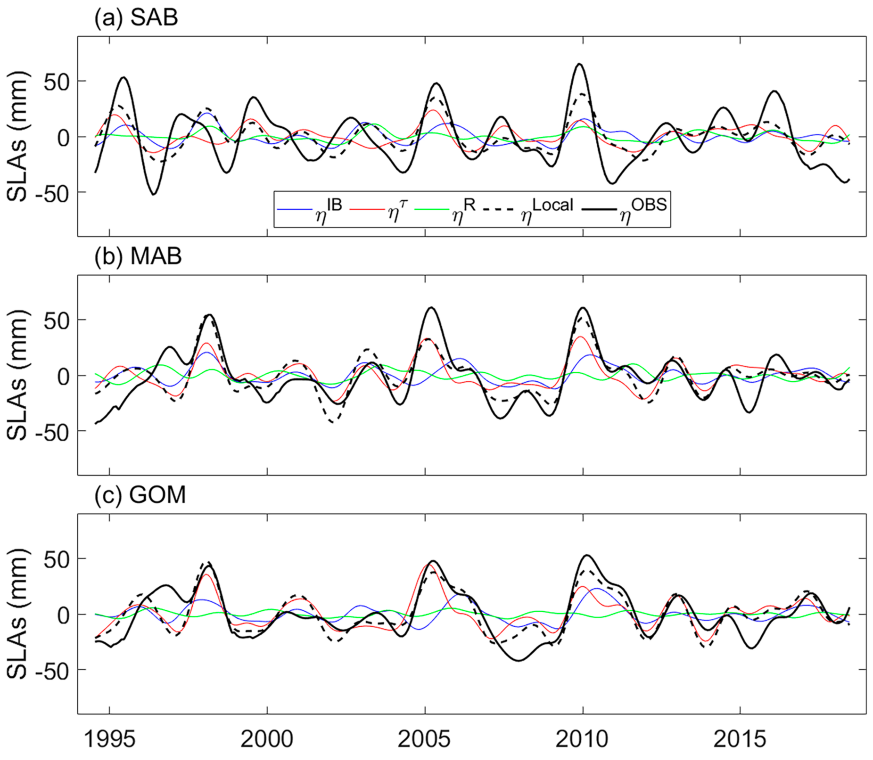

FIG. 2. Regional mean SLAs observed by tide gauges (solid black) and due to the wind stress (red), IB effect (blue), river discharges (green), and their sum that represents total local forcings (dashed black) in the (a) SAB, (b) MAB, and (c) GOM. SLAs due to local forcings were obtained from the analytical models described in section 2b, Eqs. (1)–(3).

forcings, suggesting that remote forcings are also important in driving USEC interannual SLAs.

b. *Remote forcings*

In this section, we assessed the effects of remote forcings on interannual SLAs along the USEC, without distinguishing between wind- and thermohaline-driven processes. Specifically, we examined the effects of Rossby waves from the open ocean, high-latitude signals through the northern boundary of the USEC and the GS variability.

1) FORCING FROM THE OPEN OCEAN

To understand how the open-ocean SLAs may affect coastal SLAs, we calculated lead–lag correlations between SLAs at the westernmost points of the open ocean (color dots of Fig. 3a) and SLAs along the optimal paths of westward propagation (sections b–d shown in Fig. 3a). The theoretical basis for using the optimal paths (defined in Fig. 3) is provided by Wise et al. (2018), who showed that portions of open-ocean sea level signals at a specific latitude can propagate across the slope to the shelf along a path that is equatorward tangentially to the streamline of gH/f (where H is the water depth); therefore, SLAs over the shelf and at the coast are skewed southward compared to the open-ocean SLAs.

Figure 3a shows that the optimal paths extend southwestward from the open-ocean points to the shelf, which is generally consistent with the conclusion of Wise et al. (2018). The open-ocean SLAs at the latitudes around Cape Hatteras (between 34° and 38°N) can penetrate onto the relatively narrow shelf (Fig. 3b; Fig. S6a, showing longitude–time plot of SLA along section b). It should be noted that only coastal SLAs south of the latitudes where the westward propagating signals reach the shelf can be affected by the open-ocean signals [Eq. (4)]. The open-ocean signals travel 6° from the east to the selected open-ocean point (blue dot in Fig. 3a) in 5 months, giving rise to a propagation speed of ~0.04 m s^{-1} at 35.4°N, which is 2 times the first-baroclinic mode Rossby wave propagation speed of 0.02 m s^{-1}. The larger observed propagation speed has been observed and attributed to spatially uniform forcing, background currents, and topography

TABLE 3. Percentages of explained sea level variance (%) by local forcings for the 1960–2019 period and the 1960–86 period averaged in the SAB, MAB, and GOM, respectively.

Region (period)	η^{τ}	η^{IB}	η^{R}	η^{Local}
SAB (1960–2019)	37.9	8.5	10.0	37.3
MAB (1960–2019)	56.0	−5.9	11.5	42.9
GOM (1960–2019)	29.5	0.2	6.6	32.3
SAB (1960–86)	42.0	0.3	5.6	43.2
MAB (1960–86)	61.0	−42.1	5.3	33.4
GOM (1960–86)	23.0	−57.9	−1.5	−12.5

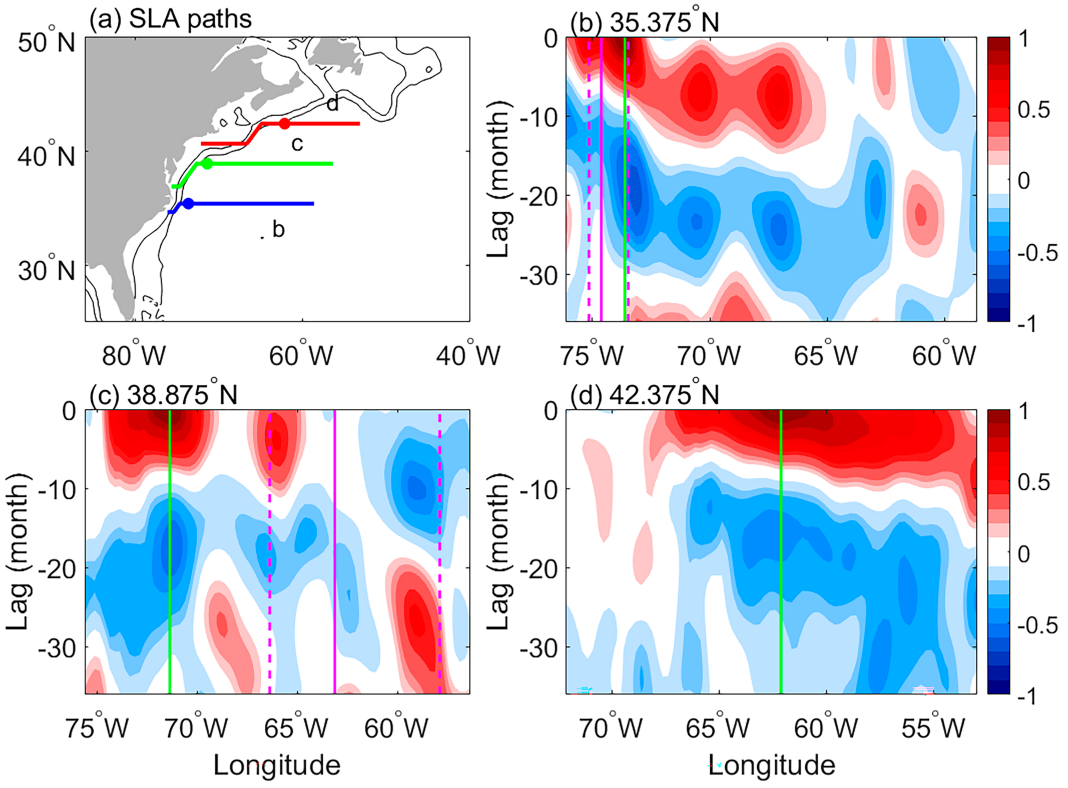

FIG. 3. (a) Horizonal sections labeled b–d along which lead–lag correlations of altimetry SLAs at the open-ocean points (colored dots) and shoreward/seaward points were calculated. The three open-ocean points are located at 35.375°N (blue dot), 38.875°N (green dot), and 42.375°N (red dot) and 1° east of 2000-m isobath. Seaward of the selected open-ocean points (colored dots), zonal sections were used; shoreward of the selected open-ocean points, the paths of maximum lagged correlations of SLAs between neighboring points were used, which represent the optimal paths of westward propagating signals. (b)–(d) The lead–lag correlations of altimetry SLAs between the open-ocean points and other points along each section. The vertical green lines in (b)–(d) mark the longitudes of the selected open-ocean points. The magenta solid and dashed lines in (b)–(d) mark the mean GS center location and GS boundaries, respectively (appendix). Correlation with a negative lag at a specific location along each section means that SLA time series at this location leads the SLA at the open-ocean point (colored dot).

in previous studies (e.g., White 1977; Killworth et al. 1997; Killworth and Blundell 2003). The open-ocean signals decelerate when encountering the eastern boundary of the GS (Fig. 3b and Fig. S6a), suggesting that the GS affects the open-ocean Rossby waves and mediates the effects of open-ocean wind stress curl forcing on the coastal SLA, which agrees with Hong et al. (2000). Our observational analysis of the open-ocean Rossby wave influence on the coastal SLA in the SAB corroborates a recent adjoint modeling study, indicating that westward propagating Rossby waves caused by open-ocean wind stress curl are important for the Charleston SLA on time scales longer than 2 months (Frederikse et al. 2022).

At latitudes between 38° and 40°N north of Cape Hatteras, the lead–lag correlations indicate eastward propagation from 67° to 58°W but the open-ocean SLAs show relatively weak direct connection with those on the shelf west of 75°W (Fig. 3c; Fig. S6b). The lack of westward propagating signals is not due to the lack of large-scale wind forcing in the open ocean (not shown). Rather, it is likely related to the eastward advection by the GS or its meandering since the eastward propagating signals shown in Fig. 3c are mainly within the GS. At latitudes between 40.5° and 43.5°N, the coastal SLAs are not correlated with SLAs at the open-ocean point east of the slope (Fig. 3d; Fig. S6c), suggesting that open-ocean SLAs within this latitude band are not directly responsible for the coastal SLAs in the northern MAB and in the GOM. As we shall see below, remote forcings from the subpolar North Atlantic Ocean play an important role in affecting coastal SLAs north of Cape Hatteras through the northern boundary of the USEC (section 3b).

We calculated the time lag δ along the southwestward paths (Fig. 3a) from the open-ocean point x_I to the shelf and then computed the open-ocean contribution with the analytical solution of Minobe et al. (2017) [second term on the right side of Eq. (4) shown in section 2b]. The open-ocean SLA η_I at x_I is chosen from altimetry data at 1° east of the continental slope. The magnitude of integrand in the second term of Eq. (4) has a decreasing trend with latitude due to the decreasing trend of SLA magnitude at open-ocean points and decreasing values of β/f^2 (Fig. 4). The open-ocean SLAs at

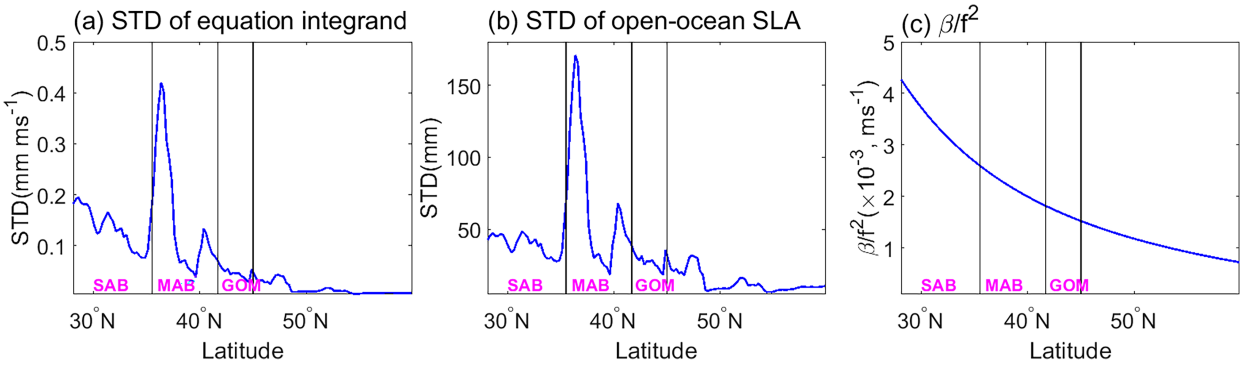

FIG. 4. (a) Standard deviations (STDs) of coastal SLAs contributed from the open ocean, measured by the integrand in the second term of Eq. (4) from 28° to 60°N. (b) STDs of SLAs at the open-ocean point, x_I, which is chosen as 1° east of the continental slope (i.e., 2000-m isobath) at each latitude. (c) β/f^2 in the second term of Eq. (4).

midlatitudes, which peak near 36.375°N, are more than 8 times that at high latitudes (north of 50°N). The large SLA magnitudes between 35° and 38°N are related to the GS because at these latitudes, the open-ocean points x_I are within the GS. At higher latitudes, the x_I positions are located west of the GS, and the open-ocean forcings represented by SLAs at x_I have small contributions to coastal SLAs along the USEC and negligible contributions north of 50°N (Fig. 4). We have tested different choices of northern boundary position y_P from 44° to 60°N and find that the open-ocean contribution is not sensitive to this choice due to the relatively small magnitude of open-ocean forcings at high latitudes. Here, we selected the northern boundary at 44.375°N on the Scotian coast because it is close to the northern boundary of the GOM and forcings north of the GOM are defined as remote forcings through the northern boundary.

As shown in Figs. 5a–c, open-ocean sea level signals mainly affect the coastal sea level in the SAB but have little influence in the MAB and GOM. In the SAB, coastal SLAs observed by tide gauges and due to open-ocean signals are significantly correlated ($r = 0.52$). A recent adjoint modeling study also suggested the important roles of westward propagating signals and the advection of the GS in the predictability of Charleston SLA (Frederikse et al. 2022). The standard deviation of η^W is 5.9 mm and explains 19% variance of observed coastal SLAs averaged in the SAB (Tables 1 and 2). The open-ocean forcing accounts for little sea level variance in the MAB and GOM, which is consistent with the lack of westward propagating signals from the open-ocean points that can reach the coasts in these regions (Fig. 3).

Note that while calculating the impact of open-ocean forcing along sections b–d is physically more reasonable (Wise et al. 2018) compared to along the zonal paths, we obtain similar results using the zonal paths as in Minobe et al. (2017) (not shown). This is because we need to perform meridional integration along the western boundary from y to y_P in Eq. (4) for both the zonal and optimal paths. The results, after meridional integration with time lag δ calculated along both zonal and optimal paths, are similar.

2) FORCING FROM THE NORTHERN BOUNDARY

We estimated the contribution of remote forcing via the northern boundary to the USEC sea level with the first term on the right side of Eq. (4). Figures 5d–f show that η^N is significantly correlated with the observed coastal sea level in the MAB ($r = 0.61$) and GOM ($r = 0.68$), but the effect of η^N is much weaker in the SAB ($r = 0.27$). The percentage of variance explained by the remote forcing through the northern boundary generally decreases from north to south due to the decrease of $f(y)$ and also due to friction in the real ocean.

SLAs at the northern boundary of our USEC domain, which is located at the Scotian coast, can result from local forcings and remote forcings from the north and east. First, we examined the influence of local alongshore wind stress on the SLA at the northern boundary location using Eq. (2) (section 2b). The local alongshore wind stress explained only a few percent of the variance in the observed SLA at the northern boundary location, so this effect can be ignored.

Remote forcings from the north and east could be important for the SLAs at the northern boundary, as indicated by the lead–lag correlations between SLAs at the northern boundary location and those at other grid points (Fig. 6). When the temporal lag is 0, the correlations suggest that the USEC SLAs are coherent north of Cape Hatteras, from the MAB to the Scotian shelf (Fig. 6f). This coherence is seen from lag = −6 months to lag = 3 months (Figs. 6d–g), suggesting that SLAs with the same sign can persist for ~9 months. In addition, SLAs at the northern boundary location of the USEC are influenced by sea level signals off the coasts of Labrador and Newfoundland, a region where the offshore Labrador Current is located (Wang et al. 2015), as shown by their positive correlations when SLAs off the Labrador and Newfoundland coasts lead by 6 months (Fig. 6d). It is also noted that SLAs southeast of the Greenland propagate slowly in counterclockwise direction to the Grand Banks first along the 2000-m isobath and then along the continental slope (between 200- and 2000-m isobaths) in the Labrador Sea where the slope becomes steep (Figs. 6i–l). It takes about 30 months for the SLAs to travel from southeast of the Greenland to the Grand Banks (Figs. 6a–k). On the other

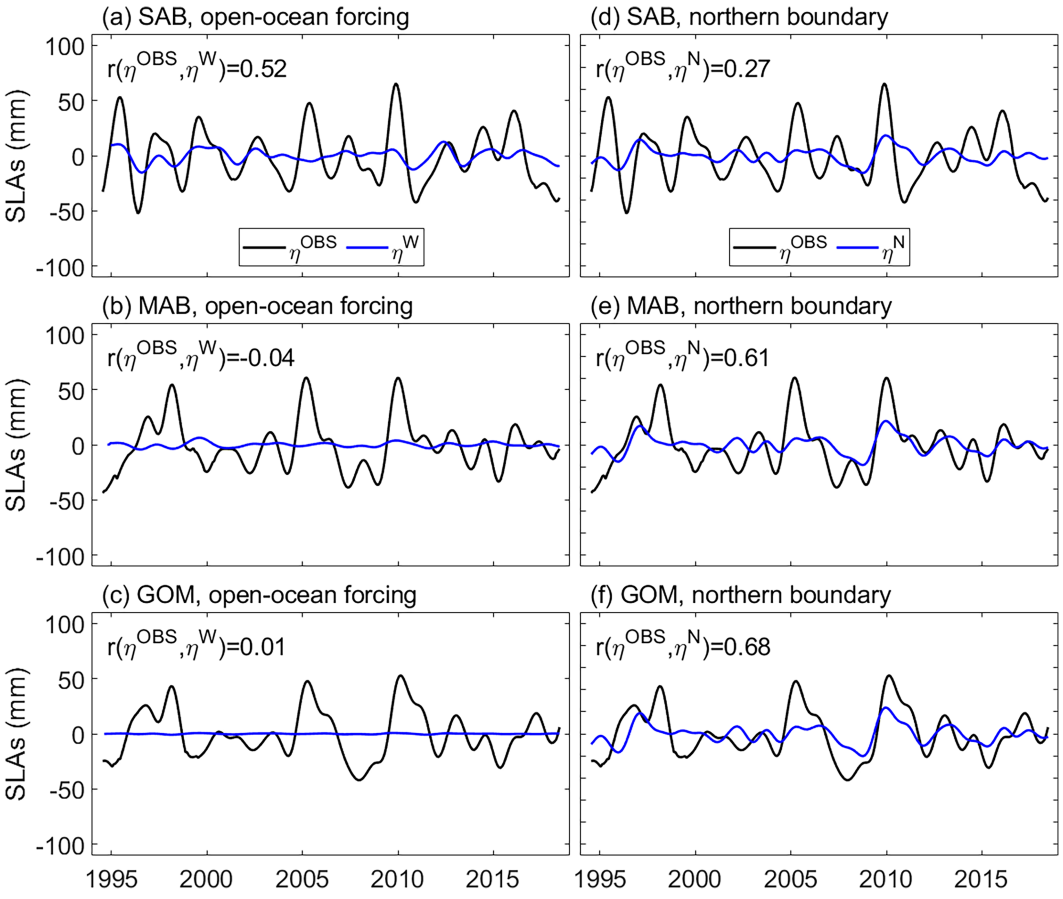

FIG. 5. Regional mean coastal SLAs observed by tide gauges (solid black) and due to open-ocean sea level signals propagating westward along a southwestward path [blue; estimated with the second term on the right side of Eq. (4)] in the (a) SAB, (b) MAB, and (c) GOM. Regional mean coastal SLAs from tide gauges (solid black) and due to sea level signals from the northern boundary at 44.375°N on the Scotian coast [blue; estimated with the first term on the right side of Eq. (4)] in the (d) SAB, (e) MAB, and (f) GOM. Correlations between tide-gauge-observed SLAs and SLAs due to remote forcings in each region are shown in the upper-left part of each panel.

hand, SLAs in the open ocean east of the Grand Banks propagate westward to the Grand Banks, intensify over the Grand Banks, and subsequently translate southwestward to the Scotian shelf (Figs. 6f–l). Therefore, SLAs at the northern boundary of our USEC domain are influenced primarily by remote forcings from the Grand Banks to the Scotian shelf with some contribution from the east of the Grand Banks and from the subpolar North Atlantic off the Labrador and Newfoundland coasts and southeast of Greenland. These results corroborate the recent adjoint sensitivity tests showing that wind and buoyancy forcings in the subpolar North Atlantic may affect the sea level at Nantucket Island in the MAB through slow advective processes (Wang et al. 2022).

To further illustrate the influence of remote forcings on SLAs at the northern boundary of our USEC domain, we calculated lead–lag correlations between SLAs at the northern boundary (44.375°N at the Scotian coast) and along the horizontal line showing in Fig. 7. Correlations along the zonal section from the open ocean east of the Grand Banks to the Scotian coast (at 44.375°N) indicate that SLAs in the open ocean east of the Grand Banks may propagate westward to affect SLAs on the Grand Banks and subsequently on the Scotian coast. The connection of SLAs between the open ocean (east of the 2000-m isobath) and the Grand Banks, however, is weak (Fig. 7b), indicating that forcings over the Grand Banks are important in affecting the northern boundary SLA at the Scotian coast. A Hovmöller diagram of satellite SLAs along the section shows that SLAs in the open ocean are stronger and noisier than those on the Grand Banks (Fig. 8a) because the open ocean east of the Grand Banks lies at the confluence of the southward flowing Labrador Current and the northward flowing North Atlantic Current where eddies are often generated (Gonçalves Neto et al. 2021). Note that sea level signals east of the Grand Banks can propagate westward to the Grand Banks (e.g., years 2000, 2010, and 2013), even though the eddies can obscure the propagating signals.

To further demonstrate the importance of wind stress forcing over the Grand Banks, we used a reduced-gravity Rossby wave model (e.g., Qiu and Chen 2010) to estimate the wind stress–induced SLAs along the zonal section at 44.375°N (Fig. 7a):

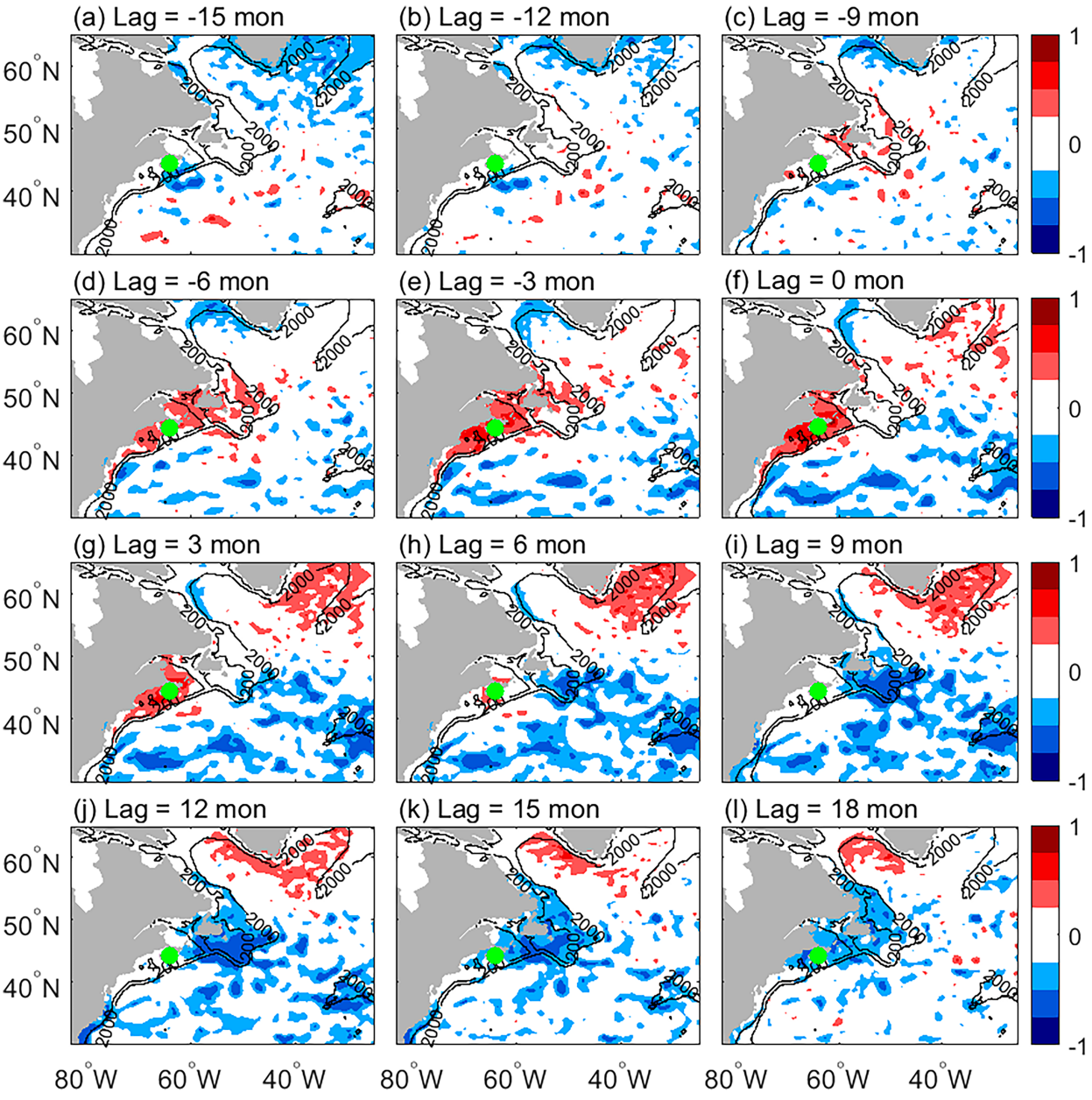

FIG. 6. Lead–lag correlation maps between altimetry SLAs at the northern boundary (green dot) of the USEC domain and those at other locations. Positive (negative) lag of n months means that SLAs at the northern boundary lead (lag) SLAs at other locations by n months. Black lines represent the 200- and 2000-m isobaths. Note that the region between the 200- and 2000-m isobaths represents the continental slope and remote sea level signals from southeast of Greenland tend to propagate along the continental slope.

$$\frac{\partial h}{\partial t} - c_r \frac{\partial h}{\partial x} = -\frac{g' \mathbf{k} \cdot \nabla \times \boldsymbol{\tau}}{\rho_0 g f} - \epsilon h, \tag{6}$$

where h is the SLA, c_r is the Rossby wave propagation speed, g' is the reduced gravity parameter, $\mathbf{k}$ is the unit vector in the vertical direction, $\boldsymbol{\tau}$ is the wind stress vector, ρ_0 is the seawater density, g is the acceleration of gravity, and ϵ is a damping coefficient. Integrating Eq. (6) from the eastern boundary westward yields

$$h = h\left(x_e, t + \frac{x - x_e}{c_r}\right)\exp\left[\frac{\epsilon(x - x_e)}{c_r}\right] + \frac{g'}{\rho_0 g f c_r}\int_{x_e}^{x} \mathbf{k} \cdot \nabla \times \boldsymbol{\tau}\left(x', t + \frac{x - x'}{c_r}\right)\exp\left[\frac{\epsilon(x - x')}{c_r}\right]dx'. \tag{7}$$

Here, the first term on the right side of Eq. (7) represents the open-ocean SLA at the eastern boundary of a selected section, x_e

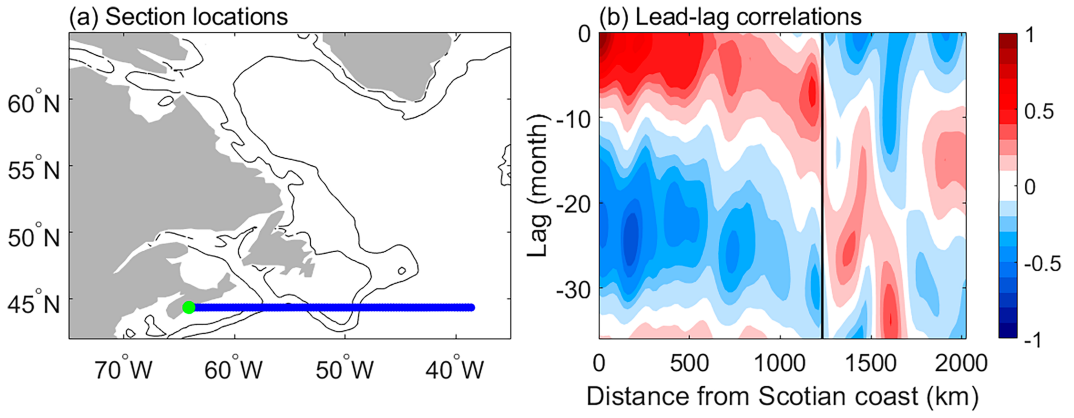

FIG. 7. (a) Horizontal section along which lead–lag correlations between satellite altimetry SLAs at the northern boundary of our USEC domain (44.375°N at the Scotian coast and marked by green dots) and other selected spatial points were calculated. Black lines represent the 200- and 2000-m isobaths. (b) Lead–lag correlations between SLAs at the northern boundary [green dot in (a)] and points along the section shown in blue line of (a). Correlation with a negative lag at a specific location means that SLA time series at this location leads SLA at the northern boundary (green dot). The black solid line in (b) marks the location of 2000-m isobath east of the Grand Banks at 44.375°N.

located at the easternmost point of the zonal section in Fig. 7a (10° east of the 2000-m isobath), and the second term represents the wind stress curl forced SLA from x_e to any location x. We determined $c_r = 0.05$ m s^{-1}, $g' = 0.05$ m s^{-2}, and $\epsilon = (1/3)$month^{-1} empirically by minimizing the variance of difference between observed and modeled SLAs. The relatively large damping coefficient, which parameterizes negative feedback processes on SLAs including dissipation (Qiu et al. 1997), suggests the importance of local damping on sea level variability. The propagation speed is close to the estimated speed of 0.06 m s^{-1} based on the lead–lag correlations (Fig. 7b) but is much faster than the first-baroclinic mode Rossby wave speed of 0.006 m s^{-1}, which might be related to the topography that is not considered in this model (e.g., Tailleux and McWilliams 2001; Tailleux 2003). This model is used to demonstrate the role of wind stress curl and sea level signals from east of the Grand Banks; the nature of the faster propagation speed is not examined here.

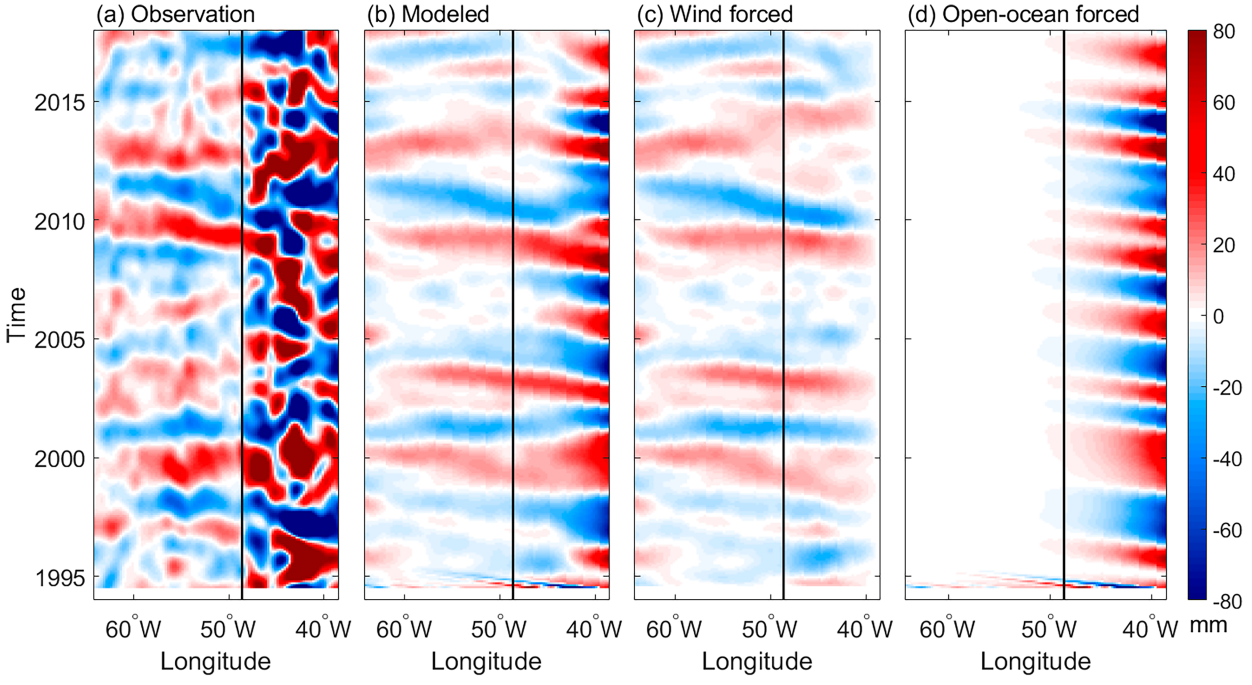

FIG. 8. Observed and modeled SLAs along the zonal section from the Scotian shelf to the Grand Banks (the zonal section at 44.375°N in Fig. 7a). The black solid lines mark the locations of 2000-m isobath east of the Grand Banks at 44.375°N.

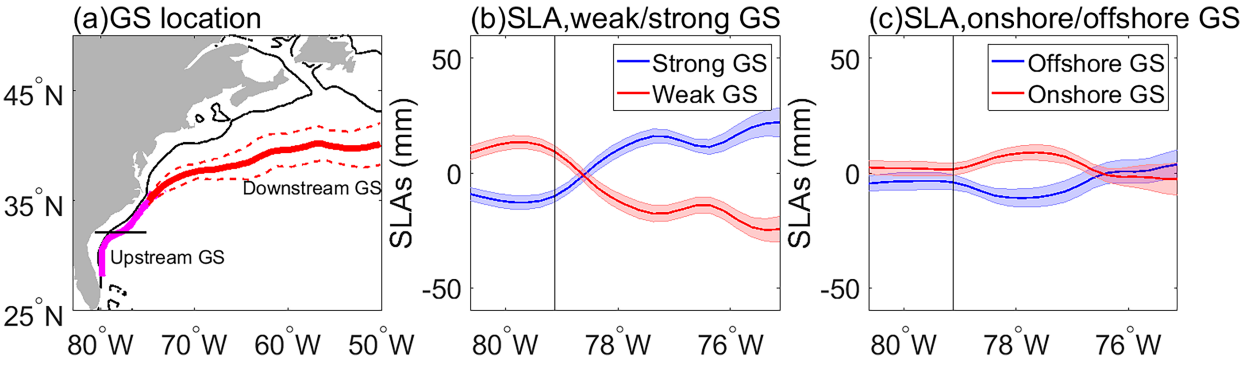

FIG. 9. (a) Mean locations of the Gulf Stream (GS) south (magenta) and north (red) of Cape Hatteras. The dashed lines represent two standard deviations of GS locations away from the mean GS locations. The horizontal black line is the zonal section at 32.125°N along which composite SLAs were estimated and shown in (b) and (c). The black contour indicates the 200-m isobath. (b) Composite interannual SLAs (mm) along the zonal section shown in (a) when the upstream GS is stronger (blue) and weaker (red) than the mean strength. (c) Composite interannual SLAs (mm) along the zonal section shown in (a) when the upstream GS is onshore (red) and offshore (blue) of the mean GS position. The shadings in (b) and (c) denote the 90% confidence level of the composite mean SLAs. The vertical black lines indicate the location of the 200-m isobath. The SLA composites on the shelf are significantly different ($p \leq 0.1$) between periods with the strong upstream GS and periods with the weak upstream GS, while the SLA composites on the shelf are not significantly different ($p > 0.1$) between periods with the offshore and onshore upstream GS.

The modeled SLAs can account for more than 15% of observed sea level variance from the Scotian shelf to the Grand Banks (62°–50°W) (Figs. 8a,b). As expected, the reduced gravity model is less successful when approaching the coast (west of 62°W) and coastal dynamics such as coastal trapped waves could be responsible for the redistribution of sea level signals reaching the coast. Wind stress curl over the Grand Banks is indeed important for generating the SLAs and accounts for almost all the 15% sea level variance explained by the Rossby wave model between 62° and 50°W (Fig. 8c). In comparison, the open-ocean forcing from 10° east of the Grand Banks is less important since the sea level signals are largely damped as they approach the Grand Banks, with the empirical damping rate of $\epsilon = (1/3)\text{month}^{-1}$ in the simple Rossby wave model (Fig. 8d). A high-resolution ocean general circulation model that can accurately simulate the USEC sea level and North Atlantic Ocean circulation is needed to achieve more accurate depictions of the relative importance of remote forcings from the subpolar North Atlantic, east of the Grand Banks, and wind stress curl from the Grand Banks to the Scotian shelf in affecting the USEC SLAs.

Previous correlation analyses (e.g., Frederikse et al. 2017; Dangendorf et al. 2021) indicate that the interannual-to-decadal coastal SLAs in the GOM and the MAB are related to the open-ocean steric SLAs west of the Labrador Sea and east of the Grand Banks; our analysis during the satellite altimetry era suggests that wind stress curl from the Grand Banks to the Scotian shelf can also be important in affecting the coastal SLAs in the GOM and MAB through the northern boundary of our USEC domain.

3) VARIABILITY OF THE GULF STREAM

The theoretical model shown by Eq. (4) only takes into account the influence of westward propagating signals from the open ocean and remote signals through the northern boundary on the USEC SLA. The coastal SLAs that cannot be accounted for by the theoretical models that assess both the local and remote forcings are partly related to GS variability. The effects of the GS were examined using the regression model [Eq. (5) of section 2b].

(i) Relation between the GS variability and coastal SLA

South of Cape Hatteras, the GS strength and location can directly affect coastal SLAs because the GS flows just offshore of the shelf edge (Fig. 9a). An anticorrelation between the upstream GS strength and the coastal SLAs is seen in the composite SLAs (Fig. 9b), and the correlation coefficients are statistically significant only in the SAB ($p \leq 0.1$; Fig. S7). However, the SLA composites on the shelf are not significantly different ($p > 0.1$) between periods with offshore upstream GS and periods with onshore upstream GS (Fig. 9c) and the correlations between the upstream location and coastal SLAs are not statistically significant ($p > 0.1$; Fig. S7) at most tide gauges, so the effect of the upstream GS location is weak. Therefore, the influence of zonal (east–west) shift of the upstream GS location on the coastal SLAs is not considered further. The influence of upstream GS on coastal SLAs (η^{UpGS}) was assessed by regressing coastal SLAs in the SAB (with the local and remote forcing effects estimated from analytical models removed) onto the upstream GS strength index [Eq. (5) of section 2b], which accounts for 0%–39.3% of sea level variance at tide-gauge locations in the SAB.

By contrast, the meridional (north–south) shift of the downstream GS has a significant positive correlation with coastal SLAs at four out of seven tide gauges in the SAB, but it is anticorrelated with the coastal SLAs north of Cape Hatteras in the MAB and GOM and the correlations are not significant ($p > 0.1$) (Fig. S7). The correlations between the downstream GS strength and the coastal SLAs are statistically insignificant at most tide gauges, which is consistent with recent studies (e.g., Dong et al. 2019). Therefore, the impact of the downstream GS strength on coastal SLAs is not considered. The influence of the

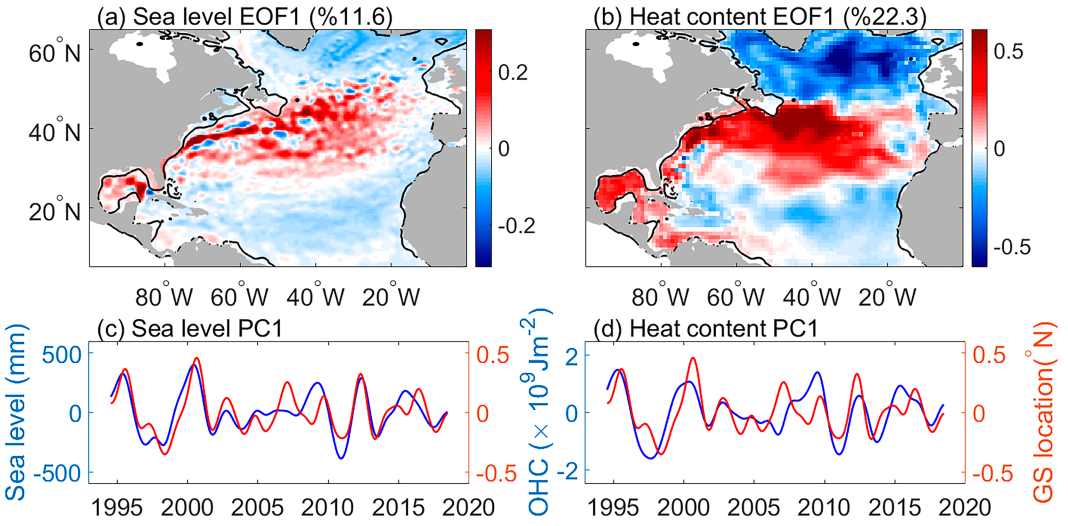

FIG. 10. The leading EOF (EOF1) of (a) interannual SLAs from satellite altimeter data and (b) in situ–based ocean heat content (OHC) anomalies in the upper 2000 m. The percentage values represent explained variance by the leading EOF. Black contours in (a) and (b) indicate the 200-m isobath. The principal component (PC1) of the leading EOF mode of (c) interannual SLAs and (d) OHC anomalies in the upper 2000 m (blue lines). The red lines in (c) and (d) represent the interannual variability of the downstream GS location index.

downstream GS on coastal SLAs (η^{DownGS}), therefore, is linked only to its north–south shift of location, which was assessed by regressing coastal SLAs in the SAB (with the local and remote forcing effects estimated from the analytical models removed) onto the downstream GS location index, and explains 3.6%–19.6% sea level variance. Note that the meridional location of the downstream GS is not significantly correlated with the upstream GS strength ($r = -0.37$; $p > 0.1$). The GS-induced sea level, $\eta^{\mathrm{GS}} = \eta^{\mathrm{UpGS}} + \eta^{\mathrm{DownGS}}$, explains 22.7% of variance for SLA averaged in the SAB (Table 1), with the standard deviation of η^{GS} being one-third of the observation (Table 2).

(ii) Relevant mechanism

Although correlations between the meridional shift of the GS and coastal SLAs are significant in the SAB, the physical processes behind the correlations have not been discussed in previous studies. In this study, we provided the physical causes for the linkage between the downstream GS location and coastal SLAs.

The leading empirical orthogonal function mode (EOF1) of interannual SLA exhibits a tripole pattern with the subtropical–midlatitude band having the opposite sign to the tropical and subpolar bands (Fig. 10a), a pattern that has been linked to the NAO and to interannual SLAs along the USEC [see the review by Han et al. (2017) and references therein]. The leading principal component (PC1) is significantly correlated with the meridional shift of the downstream GS location ($r = 0.79$; Fig. 10c), suggesting that the meridional shift in the downstream GS primarily reflects the large-scale ocean circulation change. The sea level tripole pattern is associated with a similar pattern of OHC in the upper 2000 m (Fig. 10b), consistent with Dangendorf et al. (2021); and PC1 of OHC is highly correlated with PC1 of sea level ($r = 0.89$) as well as the meridional shift of the downstream GS ($r = 0.68$) (Fig. 10d). Therefore, the significant positive correlations between the meridional shift in the downstream GS and coastal SLAs in the SAB found in previous studies reflect remote forcing from the open ocean. Although Volkov et al. (2019) indicated that the tripole pattern of sea level and heat content is related to the AMOC, the tripole pattern is also associated with the meridional shift of the downstream GS.

The linkages between the meridional shift of the downstream GS and sea level, OHC, and surface wind forcing were further examined with composite analysis, showing a northward shift of the downstream GS being associated with higher sea level and OHC in the SAB (Fig. 11). The sea level and OHC variability are closely related to the wind stress anomalies, which are cyclonic (anticyclonic) in the western (eastern) subtropical basin (Fig. 11a). The cyclonic winds in the western subtropical basin cause Ekman mass divergence from the center of the cyclonic winds and convergence along the USEC, raising sea level in the SAB. When temporal lags of a few months were considered in the wind stress composite (with wind leading sea level), the wind composite pattern does not exhibit a significant change. In addition, the cyclonic wind pattern is close to the SAB; therefore, no temporal lags were considered in the wind composite analysis with monthly data. By contrast, the SLAs and OHC anomalies have opposite signs north of Cape Hatteras in the MAB and GOM, suggesting that coastal SLAs in these regions, which are not significantly correlated with the downstream GS location as mentioned earlier, cannot be explained by OHC anomalies associated with the meridional shift of the downstream GS location.

4) CONTRIBUTION FROM ALL REMOTE FORCINGS

The coastal SLAs induced by the westward propagating open-ocean signals, variability at the northern boundary, and the remote forcings associated with the GS variability are

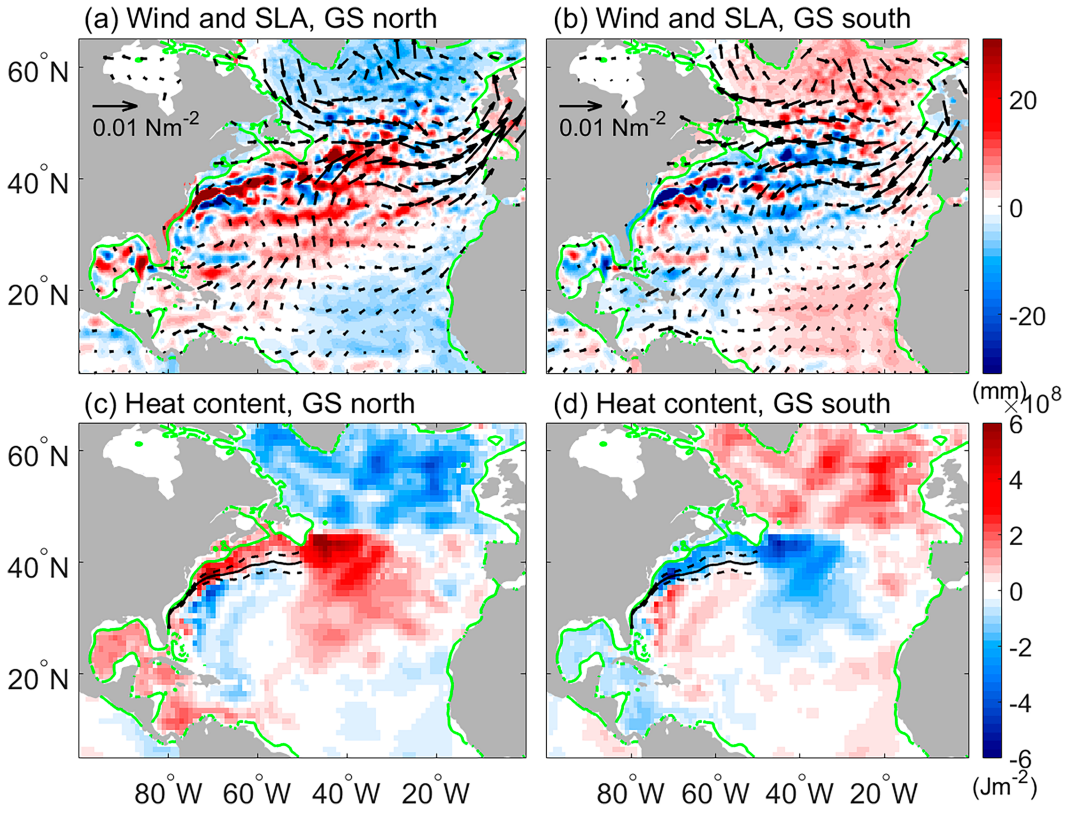

FIG. 11. Composite maps of interannual SLAs from satellite observations (color shading) and ERA5 reanalysis surface wind stress anomalies (vectors) from 1993 to 2019 when the downstream GS is shifted to (a) north of its mean position and (b) south of its mean position. Also shown are composite OHC anomalies in the upper 2000 m (color shading) when the downstream GS is shifted to (c) north of its mean position and (d) south of its mean position. The black solid and dashed lines in (c) and (d) represent mean locations of the GS and two standard deviations of GS locations away from the mean GS locations, respectively. The green contour indicates the 200-m isobath.

represented by the linear superposition of the individual effects, $\eta^{\text{Remote}} = \eta^{N} + \eta^{W} + \eta^{\text{GS}}$.

The total effect of remote forcings explains 45.7%, 28.5%, and 37.7% variance of sea level averaged in the SAB, MAB, and GOM, respectively (Table 1). The GS variability and westward propagating signals from the open ocean are the most important remote forcings in the SAB, while the sea level variability from the northern boundary at the Scotian coast is the most important remote forcing in the MAB and GOM. In addition, the magnitude of coastal SLAs induced by remote forcings is larger in the SAB than that in the MAB and GOM. For the coastal SLAs averaged in the SAB, the effect of remote forcings is comparable to that of local forcings, whereas local forcings are much larger than remote forcings in causing coastal SLAs averaged in the MAB and GOM (Table 2).

c. *Total effect: Local plus remote forcings*

The locally driven coastal SLAs at interannual time scale are highly correlated with the tide-gauge observations throughout the USEC, with correlations ranging from 0.70 in the SAB to 0.82 in the GOM, and increase in magnitude from the SAB (STD = 13.5 mm) to the GOM (STD = 18.2 mm; Fig. 12). This result is different from the small role of local forcings in the SAB on decadal time scale shown by Hong et al. (2000). The remotely driven coastal SLAs are also significantly correlated with the observations with the highest correlation coefficient of 0.70 in the SAB and lowest of 0.54 in the MAB (Fig. 12). The combined effects of local and remote forcings on interannual SLAs of the USEC, $\eta^{\text{Total}} = \eta^{\text{Local}} + \eta^{\text{Remote}}$, have comparable magnitudes as the observations and explain 77.8%, 68.1%, and 80.4% variance of SLAs averaged in the SAB, MAB, and GOM, respectively (Table 1). The estimated total coastal SLAs (local + remote) account for the majority of USEC interannual SLAs and agree well with the tide-gauge observations, with correlation coefficients ranging from 0.84 to 0.91 (Fig. 12). The good agreements between the observed and estimated total interannual SLAs along the USEC demonstrate that our analytical models assisted by the statistical method can capture the major processes that determine the USEC SLAs and thus are suitable for our purpose of assessing the relative importance of local and remote forcings.

4. Conclusions and discussion

In this study, we quantified the contributions of the local and remote forcings to the interannual SLAs along the USEC

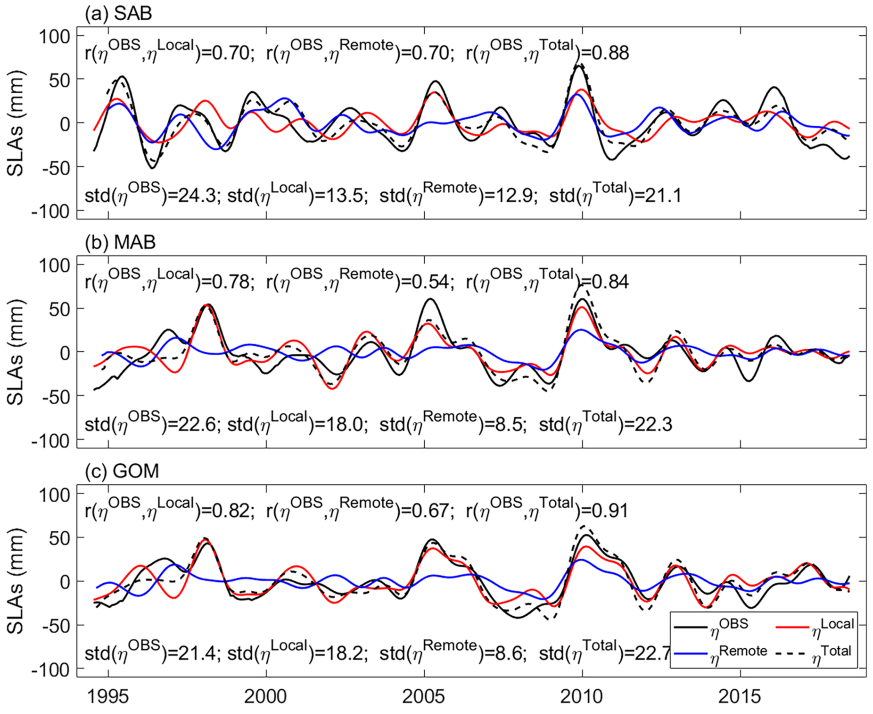

FIG. 12. Regional mean coastal SLAs observed by tide gauges (solid black), due to the local forcings (red), due to the remote forcings (blue), and due to the total forcings (dashed black) in the (a) SAB, (b) MAB, and (c) GOM. Correlations between tide-gauge-observed SLAs and SLAs due to local forcings, remote forcings, and total forcings in each region are shown in the upper part of each panel. Standard deviations (std; mm) of observed and estimated SLAs driven by local and remote forcings are shown in the lower part of each panel.

during the satellite altimetry period of 1993–2019 with analytical models assisted by the statistical method. The local forcings include alongshore wind stress, atmospheric sea level pressure through the IB effect, and river discharges, explaining 47%–66.8% sea level variance along the USEC (Table 1), with larger contributions north of Cape Hatteras in the MAB (60.4%) and GOM (66.8%) than south of Cape Hatteras in the SAB (47%; Tables 1 and 2; Fig. 2). The remote forcings include the westward-propagating signals from the open ocean, variability through the northern boundary, and the GS variability, explaining 28.5%–45.7% of coastal sea level variance, with the highest (lowest) occurring in the SAB (MAB) and 37.7% in the GOM (Table 1). The GS variability and westward propagating signals from the open ocean are more important for coastal SLAs in the SAB, while remote forcing from the northern boundary at the Scotian coast is more important in the MAB and the GOM. Remote forcings from the open ocean and the northern boundary together with the GS variability play a comparable role as local forcings in driving coastal interannual SLAs in the SAB but local forcings are more important than remote forcings in the MAB and GOM (Tables 1 and 2; Fig. 12).

In addition to quantifying the contributions of local and remote forcings to the interannual SLAs in different regions of the USEC, this study yields the following new findings:

1) The coastal sea level in the SAB is affected by the upstream GS strength related to geostrophic balance and by basin-scale wind stress curl anomalies, which are linked to the meridional shift of the downstream GS location (Figs. 9–11). This result provides a physical interpretation for the correlation between coastal SLAs in the SAB and the meridional shift of the downstream GS location found by previous studies.
2) Regarding the remote impacts, the open-ocean sea level signals from 35° to 38°N are the most important causes for coastal SLAs in the SAB (Figs. 3 and 5), while sea level signals from the Grand Banks to the Scotian shelf are important for causing coastal SLAs in the MAB and the GOM via slow propagation through the northern boundary of the USEC with a propagation speed of 0.06 m s^{-1} (Figs. 5–8). Wind stress curls from the Grand Banks to the Scotian shelf are important for driving SLAs over these regions (Fig. 8), in addition to the contributions from remote SLAs originated from the subpolar North Atlantic (off the Labrador and Newfoundland coasts and southeast of Greenland) and, to a lesser extent, from east of the Grand Banks (Figs. 6–8). The effect of local alongshore wind at the northern boundary location of the USEC is weak.

Further quantifications of the relative importance of remote wind and buoyancy forcings from the southeast of Greenland, the Labrador Sea, and east of the Grand Banks versus wind

forcing from the Grand Banks to the Scotian Shelf in causing USEC SLAs will be conducted with numerical model experiments in our future work. For this purpose, high-resolution numerical model experiments that can adequately resolve continental shelf and slope with reliable surface wind and buoyancy forcing fields are needed in order to achieve more accurate quantifications of the roles played by local and remote forcings in causing interannual sea level variability in different regions of the USEC. Models, however, have biases, which can make accurate simulations of USEC sea level challenging.

This study suggests that remote forcings from the open ocean to the east have weak influence on interannual SLAs in the coasts of the MAB and the GOM, which is likely due to the lack of westward propagating signals north of 38°N that pass through the continental slope and the broad shelf. The lack of westward propagating signals, however, is not due to the lack of large-scale wind forcing in the open ocean (now shown). Rather, the downstream GS might block the westward propagating signals generated east of the GS, and the open ocean between the MAB and the GS is narrow so that locally driven SLAs in the narrow open ocean may not form significant westward propagating Rossby waves. Detailed studies are needed to fully understand the causes of the lack of open-ocean impacts from the east on interannual SLAs along the USEC north of Cape Hatteras.

Finally, this paper focused on studying the interannual coastal SLAs (1.5–8 years); however, decadal SLAs are also important for near-term projections of coastal sea level. Longer observational records and model simulations are needed to understand the causes for decadal sea level variability along the USEC.

Acknowledgments. We thank Christopher G. Piecuch, Shoshiro Minobe, and one anonymous reviewer for their constructive comments and suggestions. YZ and WH were supported by the NOAA Office of Oceanic and Atmospheric Research Climate Program Office (CPO) NA20OAR4310480 and NASA OSTST Award 80NSSC21K1190. A portion of the work was completed when WH was visiting the International Space Science Institute (ISSI), Bern, Switzerland. She thanks the Johannes Geiss Fellowship from ISSI for providing travel support and Dr. Anny Cazenave for stimulating discussion. MA and SS were supported by NOAA NA20OAR4310480 and thank the support of the NOAA/CPO/Climate Variability and Predictability Program.

Data availability statement. The tide-gauge monthly mean sea level was obtained from PSMSL (Holgate et al. 2013), retrieved from http://www.psmsl.org/data/obtaining/. ERA5 monthly atmospheric sea level pressure, wind stress (Hersbach et al. 2019), and the DT2018 gridded sea level dataset (Taburet et al. 2019) were provided by the C3S Climate Data Store (https://cds.climate.copernicus.eu/#!/home). The monthly river discharges along the USEC were obtained from USGS water data for the nation (https://waterdata.usgs.gov/nwis). The gridded product of OHC for the 0–2000-m layer (Cheng et al. 2017) was retrieved from http://www.ocean.iap.ac.cn/pages/dataService/dataService.html?languageType=en&navAnchor=dataService.

APPENDIX

Estimation of GS Location and Strength

The GS location and strength were derived from the altimetry data. The GS was separated into upstream and downstream components, located to the south and north of Cape Hatteras, respectively. Following previous studies (e.g., Dong et al. 2019), for the downstream GS, we found the initial estimates of GS center locations based on the sea surface height (SSH) contour value of 0.25 m located north of Cape Hatteras (75°–50°W) and adjusted the initial estimates by finding the locations with maximum speed within a meridional distance of 1° from the initial locations. The maximum speed was defined as the strength of the downstream GS. For the upstream GS, we found the initial estimates of GS center locations based on the SSH contour of 0.4 m south of Cape Hatteras (28°–36°N) and adjusted the initial estimates by finding the locations with maximum speed within a zonal distance of 1° from the initial locations. Similarly, the maximum speed was defined as the strength of the upstream GS. The boundaries of the GS were defined as the places where the current speed is e^{-1} times the maximum speed of the GS around the GS center locations.

It should be noted that the GS strength was approximated by the surface current speed, which could be different than the vertically integrated total volume transport. Volkov et al. (2020) compared cross-stream sea surface height gradients with the Florida Current (upstream of the Gulf Stream) volume transport derived from cable measurements and ship sections, indicating that satellite altimetry reproduces the interannual variability of the Florida Current transport fairly well. The GS strength derived from the altimetry data was thus used in this study, and the influence of using total volume transport will be examined in a future study.

REFERENCES

Andres, M., G. G. Gawarkiewicz, and J. M. Toole, 2013: Interannual sea level variability in the western North Atlantic: Regional forcing and remote response. *Geophys. Res. Lett.*, **40**, 5915–5919, https://doi.org/10.1002/2013GL058013.

Bingham, R. J., and C. W. Hughes, 2009: Signature of the Atlantic meridional overturning circulation in sea level along the east coast of North America. *Geophys. Res. Lett.*, **36**, L02603, https://doi.org/10.1029/2008GL036215.

Blaha, J. P., 1984: Fluctuations of monthly sea level as related to the intensity of the Gulf Stream from Key West to Norfolk. *J. Geophys. Res.*, **89**, 8033–8042, https://doi.org/10.1029/JC089iC05p08033.

Cazenave, A., and Coauthors, 2022: Sea level along the world's coastlines can be measured by a network of virtual altimetry stations. *Commun. Earth Environ.*, **3**, 117, https://doi.org/10.1038/s43247-022-00448-z.

Chen, N., G. Han, and X.-H. Yan, 2020: Similarity and difference in interannual sea level variations between the Mid-Atlantic

Bight and the Nova Scotia coast. *J. Geophys. Res. Oceans*, **125**, e2019JC015919, https://doi.org/10.1029/2019JC015919.

Cheng, L., K. Trenberth, J. Fasullo, T. Boyer, J. Abraham, and J. Zhu, 2017: Improved estimates of ocean heat content from 1960 to 2015. *Sci. Adv.*, **3**, e1601545, https://doi.org/10.1126/sciadv.1601545.

Church, J., and Coauthors, 2013: Sea level change. *Climate Change 2013: The Physical Science Basis*, T. F. Stocker et al., Eds., Cambridge University Press, 1137–1216.

Dangendorf, S., F. M. Calafat, A. Arns, T. Wahl, I. D. Haigh, and J. Jensen, 2014: Mean sea level variability in the North Sea: Processes and implications. *J. Geophys. Res. Oceans*, **119**, 6820–6841, https://doi.org/10.1002/2014JC009901.

——, T. Frederikse, L. Chafik, J. M. Klinck, T. Ezer, and B. D. Hamlington, 2021: Data-driven reconstruction reveals large-scale ocean circulation control on coastal sea level. *Nat. Climate Change*, **11**, 514–520, https://doi.org/10.1038/s41558-021-01046-1.

Diabaté, S. T., D. Swingedouw, J. J.-M. Hirschi, A. Duchez, P. J. Leadbitter, I. D. Haigh, and G. D. McCarthy, 2021: Western boundary circulation and coastal sea-level variability in Northern Hemisphere oceans. *Ocean Sci.*, **17**, 1449–1471, https://doi.org/10.5194/os-17-1449-2021.

Domingues, R., G. Goni, M. Baringer, and D. Volkov, 2018: What caused the accelerated sea level changes along the U.S. East Coast during 2010–2015? *Geophys. Res. Lett.*, **45**, 13 367–13 376, https://doi.org/10.1029/2018GL081183.

Dong, S., M. O. Baringer, and G. J. Goni, 2019: Slow down of the Gulf Stream during 1993–2016. *Sci. Rep.*, **9**, 6672, https://doi.org/10.1038/s41598-019-42820-8.

Durand, F., and Coauthors, 2019: Impact of continental freshwater runoff on coastal sea level. *Surv. Geophys.*, **40**, 1437–1466, https://doi.org/10.1007/s10712-019-09536-w.

Ezer, T., 2013: Sea level rise, spatially uneven and temporally unsteady: Why the U.S. East Coast, the global tide gauge record, and the global altimeter data show different trends. *Geophys. Res. Lett.*, **40**, 5439–5444, https://doi.org/10.1002/2013GL057952.

——, 2015: Detecting changes in the transport of the Gulf Stream and the Atlantic overturning circulation from coastal sea level data: The extreme decline in 2009–2010 and estimated variations for 1935–2012. *Global Planet. Change*, **129**, 23–36, https://doi.org/10.1016/j.gloplacha.2015.03.002.

——, 2019: Regional differences in sea level rise between the Mid-Atlantic Bight and the South Atlantic Bight: Is the Gulf Stream to blame? *Earth's Future*, **7**, 771–783, https://doi.org/10.1029/2019EF001174.

——, L. P. Atkinson, W. B. Corlett, and J. L. Blanco, 2013: Gulf Stream's induced sea level rise and variability along the U.S. Mid-Atlantic coast. *J. Geophys. Res. Oceans*, **118**, 685–697, https://doi.org/10.1002/jgrc.20091.

Field, C. B., and Coauthors, 2014: Summary for policymakers. *Climate Change 2014: Impacts, Adaptation, and Vulnerability Part A: Global and Sectoral Aspects*, C. B. Field et al., Eds., Cambridge University Press, 1–32.

Frederikse, T., K. Simon, C. A. Katsman, and R. Riva, 2017: The sea-level budget along the Northwest Atlantic coast: GIA, mass changes, and large-scale ocean dynamics. *J. Geophys. Res. Oceans*, **122**, 5486–5501, https://doi.org/10.1002/2017JC012699.

——, T. Lee, O. Wang, B. Kirtman, E. Becker, B. Hamlington, D. Limonadi, and D. Waliser, 2022: A hybrid dynamical approach for seasonal prediction of sea-level anomalies: A pilot study for Charleston, South Carolina. *J. Geophys. Res. Oceans*, **127**, e2021JC018137, https://doi.org/10.1029/2021JC018137.

Goddard, P., J. Yin, S. M. Griffies, and S. Zhang, 2015: An extreme event of sea-level rise along the northeast coast of North America in 2009–2010. *Nat. Commun.*, **6**, 6346, https://doi.org/10.1038/ncomms7346.

Gonçalves Neto, A., J. A. Langan, and J. B. Palter, 2021: Changes in the Gulf Stream preceded rapid warming of the northwest Atlantic Shelf. *Commun. Earth Environ.*, **2**, 74, https://doi.org/10.1038/s43247-021-00143-5.

Gornitz, V., S. Couch, and E. K. Hartig, 2001: Impacts of sea level rise in the New York City metropolitan area. *Global Planet. Change*, **32**, 61–88, https://doi.org/10.1016/S0921-8181(01)00150-3.

Han, W., G. A. Meehl, D. Stammer, A. Hu, B. Hamlington, J. Kenigson, H. Palanisamy, and P. Thompson, 2017: Spatial patterns of sea level variability associated with natural internal climate modes. *Surv. Geophys.*, **38**, 217–250, https://doi.org/10.1007/s10712-016-9386-y.

——, and Coauthors, 2019: Impacts of basin-scale climate modes on coastal sea level: A review. *Surv. Geophys.*, **40**, 1493–1541, https://doi.org/10.1007/s10712-019-09562-8.

Hersbach, H., and Coauthors, 2019: ERA5 monthly averaged data on single levels from 1979 to present. Copernicus Climate Change Service (C3S) Climate Data Store (CDS), accessed 2021, https://doi.org/10.24381/cds.f17050d7.

Holgate, S. J., and Coauthors, 2013: New data systems and products at the Permanent Service for Mean Sea Level. *J. Coastal Res.*, **29**, 493–504, https://doi.org/10.2112/JCOASTRES-D-12-00175.1.

Hong, B. G., W. Sturges, and A. J. Clarke, 2000: Sea level on the U.S. East Coast: Decadal variability caused by open ocean wind-curl forcing. *J. Phys. Oceanogr.*, **30**, 2088–2098, https://doi.org/10.1175/1520-0485(2000)030<2088:SLOTUS>2.0.CO;2.

Hu, A., and S. C. Bates, 2018: Internal climate variability and projected future regional steric and dynamic sea level rise. *Nat. Commun.*, **9**, 1068, https://doi.org/10.1038/s41467-018-03474-8.

——, G. A. Meehl, W. Han, and J. Yin, 2011: Effect of the potential melting of the Greenland Ice Sheet on the meridional overturning circulation and global climate in the future. *Deep-Sea Res. II*, **58**, 1914–1926, https://doi.org/10.1016/j.dsr2.2010.10.069.

Hughes, C. W., I. Fukumori, S. M. Griffies, J. M. Huthnance, S. Minobe, P. Spence, K. R. Thompson, and A. Wise, 2019: Sea level and the role of coastal trapped waves in mediating the influence of the open ocean on the coast. *Surv. Geophys.*, **40**, 1467–1492, https://doi.org/10.1007/s10712-019-09535-x.

Kenigson, J. S., W. Han, B. Rajagopalan, and M. Jasinski, 2018: Decadal shift of NAO-linked interannual sea level variability along the U.S. northeast coast. *J. Climate*, **31**, 4981–4989, https://doi.org/10.1175/JCLI-D-17-0403.1.

Killworth, P. D., and J. R. Blundell, 2003: Long extratropical planetary wave propagation in the presence of slowly varying mean flow and bottom topography. Part I: The local problem. *J. Phys. Oceanogr.*, **33**, 784–801, https://doi.org/10.1175/1520-0485(2003)33<784:LEPWPI>2.0.CO;2.

——, D. B. Chelton, and R. A. de Szoeke, 1997: The speed of observed and theoretical long extratropical planetary waves. *J. Phys. Oceanogr.*, **27**, 1946–1966, https://doi.org/10.1175/1520-0485(1997)027<1946:TSOOAT>2.0.CO;2.

Kopp, R. E., 2013: Does the mid-Atlantic United States sea level acceleration hot spot reflect ocean dynamic variability? *Geophys. Res. Lett.*, **40**, 3981–3985, https://doi.org/10.1002/grl.50781.

Li, J., and A. J. Clarke, 2005: Interannual flow along the northern coast of the Gulf of Mexico. *J. Geophys. Res.*, **110**, C11002, https://doi.org/10.1029/2004JC002606.

Li, Y., R. Ji, P. S. Fratantoni, C. Chen, J. A. Hare, C. S. Davis, and R. C. Beardsley, 2014: Wind-induced interannual variability of sea level slope, along-shelf flow, and surface salinity on the northwest Atlantic shelf. *J. Geophys. Res. Oceans*, **119**, 2462–2479, https://doi.org/10.1002/2013JC009385.

Little, C. M., C. G. Piecuch, and R. M. Ponte, 2017: On the relationship between the meridional overturning circulation, alongshore wind stress, and United States East Coast sea level in the Community Earth System Model large ensemble. *J. Geophys. Res. Oceans*, **122**, 4554–4568, https://doi.org/10.1002/2017JC012713.

——, A. Hu, C. W. Hughes, G. D. McCarthy, C. G. Piecuch, R. M. Ponte, and M. D. Thomas, 2019: The relationship between U.S. East Coast sea level and the Atlantic meridional overturning circulation: A review. *J. Geophys. Res. Oceans*, **124**, 6435–6458, https://doi.org/10.1029/2019JC015152.

McCarthy, G. D., I. D. Haigh, J. J.-M. Hirschi, J. P. Grist, D. A. Smeed, 2015: Ocean impact on decadal Atlantic climate variability revealed by sea-level observations. *Nature*, **521**, 508–510, https://doi.org/10.1038/nature14491.

Meade, R. H., and K. O. Emery, 1971: Sea level as affected by river runoff, eastern United States. *Science*, **173**, 425–428, https://doi.org/10.1126/science.173.3995.425.

Miller, L., and B. C. Douglas, 2007: Gyre-scale atmospheric pressure variations and their relation to 19th and 20th century sea level rise. *Geophys. Res. Lett.*, **34**, L16602, https://doi.org/10.1029/2007GL030862.

Minobe, S., M. Terada, B. Qiu, and N. Schneider, 2017: Western boundary sea level: A theory, rule of thumb, and application to climate models. *J. Phys. Oceanogr.*, **47**, 957–977, https://doi.org/10.1175/JPO-D-16-0144.1.

Neumann, B., A. T. Vafeidis, J. Zimmermann, and R. J. Nicholls, 2015: Future coastal population growth and exposure to sea-level rise and coastal flooding—A global assessment. *PLOS ONE*, **10**, e0118571, https://doi.org/10.1371/journal.pone.0118571.

Oppenheimer, M., and Coauthors, 2019: Sea level rise and implications for low-lying islands, coasts and communities. *IPCC Special Report on the Ocean and Cryosphere in a Changing Climate*, H.-O. Pörtner et al., Eds., Cambridge University Press, 321–445, https://doi.org/10.1017/9781009157964.006.

Piecuch, C. G., and R. M. Ponte, 2015: Inverted barometer contributions to recent sea level changes along the northeast coast of North America. *Geophys. Res. Lett.*, **42**, 5918–5925, https://doi.org/10.1002/2015GL064580.

——, S. Dangendorf, R. M. Ponte, and M. Marcos, 2016: Annual sea level changes on the North American northeast Coast: Influence of local winds and barotropic motions. *J. Climate*, **29**, 4801–4816, https://doi.org/10.1175/JCLI-D-16-0048.1.

——, K. Bittermann, A. C. Kemp, R. M. Ponte, C. M. Little, S. E. Engelhart, and S. J. Lentz, 2018: River-discharge effects on United States Atlantic and Gulf Coast sea-level changes. *Proc. Natl. Acad. Sci. USA*, **115**, 7729–7734, https://doi.org/10.1073/pnas.1805428115.

——, F. M. Calafat, S. Dangendorf, and G. Jordà, 2019: The ability of barotropic models to simulate historical mean sea level changes from coastal tide gauge data. *Surv. Geophys.*, **40**, 1399–1435, https://doi.org/10.1007/s10712-019-09537-9.

Ponte, R. M., 1992: The sea level response of a stratified ocean to barometric pressure forcing. *J. Phys. Oceanogr.*, **22**, 109–113, https://doi.org/10.1175/1520-0485(1992)022<0109:TSLROA>2.0.CO;2.

——, 2006: Low-frequency sea level variability and the inverted barometer effect. *J. Atmos. Oceanic Technol.*, **23**, 619–629, https://doi.org/10.1175/JTECH1864.1.

——, and Coauthors, 2019: Towards comprehensive observing and modeling systems for monitoring and predicting regional to coastal sea level. *Front. Mar. Sci.*, **6**, 437, https://doi.org/10.3389/fmars.2019.00437.

Qiu, B., and S. Chen, 2010: Interannual-to-decadal variability in the bifurcation of the North Equatorial Current off the Philippines. *J. Phys. Oceanogr.*, **40**, 2525–2538, https://doi.org/10.1175/2010JPO4462.1.

——, W. Miao, and P. Müller, 1997: Propagation and decay of forced and free baroclinic Rossby waves in off-equatorial oceans. *J. Phys. Oceanogr.*, **27**, 2405–2417, https://doi.org/10.1175/1520-0485(1997)027<2405:PADOFA>2.0.CO;2.

Rossby, T., C. N. Flagg, K. Donohue, A. Sanchez-Franks, and J. Lillibridge, 2014: On the long-term stability of Gulf Stream transport based on 20 years of direct measurements. *Geophys. Res. Lett.*, **41**, 114–120, https://doi.org/10.1002/2013GL058636.

Sallenger, A. H., Jr., K. S. Doran, and P. A. Howd, 2012: Hotspot of accelerated sea-level rise on the Atlantic coast of North America. *Nat. Climate Change*, **2**, 884–888, https://doi.org/10.1038/nclimate1597.

Sandstrom, H., 1980: On the wind-induced sea level changes on the Scotian Shelf. *J. Geophys. Res.*, **85**, 461–468, https://doi.org/10.1029/JC085iC01p00461.

Sweet, W., G. Dusek, D. Marcy, G. Carbin, and J. Marra, 2019: 2018 state of U.S. high tide flooding with a 2019 outlook. NOAA Tech. Rep. NOS CO-OPS 090, 31 pp., https://tidesandcurrents.noaa.gov/publications/Techrpt_090_2018_State_of_US_HighTideFlooding_with_a_2019_Outlook_Final.pdf.

——, S. Simon, G. Dusek, D. Marcy, W. Brooks, M. Pendleton, and J. Marra, 2021: 2021 state of high tide flooding and annual outlook. NOAA High Tide Flooding Rep., 28 pp., https://tidesandcurrents.noaa.gov/publications/2021_State_of_High_Tide_Flooding_and_Annual_Outlook_Final.pdf.

Taburet, G., A. Sanchez-Roman, M. Ballarotta, M.-I. Pujol, J.-F. Legeais, F. Fournier, Y. Faugere, and G. Dibarboure, 2019: DUACS DT2018: 25 years of reprocessed sea level altimetry products. *Ocean Sci.*, **15**, 1207–1224, https://doi.org/10.5194/os-15-1207-2019.

Tailleux, R., 2003: Comments on "The effect of bottom topography on the speed of long extratropical planetary waves." *J. Phys. Oceanogr.*, **33**, 1536–1541, https://doi.org/10.1175/1520-0485(2003)033<1536:COTEOB>2.0.CO;2.

——, and J. C. McWilliams, 2001: The effect of bottom pressure decoupling on the speed of extratropical, baroclinic Rossby waves. *J. Phys. Oceanogr.*, **31**, 1461–1476, https://doi.org/10.1175/1520-0485(2001)031<1461:TEOBPD>2.0.CO;2.

Thompson, P. R., and G. T. Mitchum, 2014: Coherent sea level variability on the North Atlantic western boundary. *J. Geophys. Res. Oceans*, **119**, 5676–5689, https://doi.org/10.1002/2014JC009999.

Valle-Levinson, A., A. Dutton, and J. B. Martin, 2017: Spatial and temporal variability of sea level rise hot spots over the eastern United States. *Geophys. Res. Lett.*, **44**, 7876–7882, https://doi.org/10.1002/2017GL073926.

Volkov, D. L., S.-K. Lee, R. Domingues, H. Zhang, and M. Goes, 2019: Interannual sea level variability along the southeastern seaboard of the United States in relation to the gyre-scale heat divergence in the North Atlantic. *Geophys. Res. Lett.*, **46**, 7481–7490, https://doi.org/10.1029/2019GL083596.

——, R. Domingues, C. S. Meinen, R. Garcia, M. Baringer, G. Goni, and R. H. Smith, 2020: Inferring Florida Current volume transport from satellite altimetry. *J. Geophys. Res. Oceans*, **125**, e2020JC016763, https://doi.org/10.1029/2020JC016763.

Wahl, T., S. Jain, J. Bender, S. D. Meyers, and M. E. Luther, 2015: Increasing risk of compound flooding from storm surge and rainfall for major US cities. *Nat. Climate Change*, **5**, 1093–1097, https://doi.org/10.1038/nclimate2736.

Wang, O., and Coauthors, 2022: Local and remote forcing of interannual sea-level variability at Nantucket Island. *J. Geophys. Res. Oceans*, **127**, e2021JC018275, https://doi.org/10.1029/2021JC018275.

Wang, Z., I. Yashayaev, and B. Greenan, 2015: Seasonality of the inshore Labrador current over the Newfoundland shelf. *Cont. Shelf Res.*, **100**, 1–10, https://doi.org/10.1016/j.csr.2015.03.010.

Wdowinski, S., R. Braya, B. P. Kirtmana, and Z. Wub, 2016: Increasing flooding hazard in coastal communities due to rising sea level: Case study of Miami Beach, Florida. *Ocean Coastal Manage.*, **126**, 1–8, https://doi.org/10.1016/j.ocecoaman.2016.03.002.

White, W. B., 1977: Annual forcing of baroclinic long waves in the tropical North Pacific Ocean. *J. Phys. Oceanogr.*, **7**, 50–61, https://doi.org/10.1175/1520-0485(1977)007<0050:AFOBLW>2.0.CO;2.

Wise, A., C. W. Hughes, and J. A. Polton, 2018: Bathymetric influence on the coastal sea level response to ocean gyres at western boundaries. *J. Phys. Oceanogr.*, **48**, 2949–2964, https://doi.org/10.1175/JPO-D-18-0007.1.

——, ——, ——, and J. M. Huthnance, 2020a: Leaky slope waves and sea level: Unusual consequences of the beta effect along western boundaries with bottom topography and dissipation. *J. Phys. Oceanogr.*, **50**, 217–237, https://doi.org/10.1175/JPO-D-19-0084.1.

——, J. A. Polton, C. W. Hughes, and J. M. Huthnance, 2020b: Idealised modelling of offshore-forced sea level hot spots and boundary waves along the North American East Coast. *Ocean Modell.*, **155**, 101706, https://doi.org/10.1016/j.ocemod.2020.101706.

Woodworth, P. L., M. A. M. Maqueda, V. M. Roussenov, R. G. Williams, and C. W. Hughes, 2014: Mean sea-level variability along the northeast American Atlantic coast and the roles of the wind and the overturning circulation. *J. Geophys. Res. Oceans*, **119**, 8916–8935, https://doi.org/10.1002/2014JC010520.

——, and Coauthors, 2019: Forcing factors affecting sea level changes at the coast. *Surv. Geophys.*, **40**, 1351–1397, https://doi.org/10.1007/s10712-019-09531-1.

Wu, H., 2021: Beta-plane arrested topographic wave as a linkage of open ocean forcing and mean shelf circulation. *J. Phys. Oceanogr.*, **51**, 879–893, https://doi.org/10.1175/JPO-D-20-0195.1.

Wunsch, C., and D. Stammer, 1997: Atmospheric loading and the oceanic "inverted barometer" effect. *Rev. Geophys.*, **35**, 79–107, https://doi.org/10.1029/96RG03037.

Xu, F.-H., and L.-Y. Oey, 2011: The origin of along-shelf pressure gradient in the middle Atlantic Bight. *J. Phys. Oceanogr.*, **41**, 1720–1740, https://doi.org/10.1175/2011JPO4589.1.

Yin, J., and P. B. Goddard, 2013: Oceanic control of sea level rise patterns along the east coast of the United States. *Geophys. Res. Lett.*, **40**, 5514–5520, https://doi.org/10.1002/2013GL057992.

——, M. E. Schlesinger, and R. J. Stouffer, 2009: Model projections of rapid sea-level rise on the northeast coast of the United States. *Nat. Geosci.*, **2**, 262–266, https://doi.org/10.1038/ngeo462.

Zhai, X., H. L. Johnson, and D. P. Marshall, 2014: A simple model of the response of the Atlantic to the North Atlantic Oscillation. *J. Climate*, **27**, 4052–4069, https://doi.org/10.1175/JCLI-D-13-00330.1.

Zhu, Y., W. Han, and M. A. Alexander, 2023: Nonstationary roles of regional forcings in driving low-frequency sea level variability along the U.S. east coast since the 1950s. *Geophys. Res. Lett.*, **50**, e2023GL104191, https://doi.org/10.1029/2023GL104191.

Zuo, H., M. A. Balmaseda, S. Tietsche, K. Mogensen, and M. Mayer, 2019: The ECMWF operational ensemble reanalysis-analysis system for ocean and sea ice: A description of the system and assessment. *Ocean Sci.*, **15**, 779–808, https://doi.org/10.5194/os-15-779-2019.